MODELING THE ROLES OF MICRO-DEFORMATION MECHANISMS ON THE DEFORMATION RESPONSE OF HIGH-MANGANESE AUSTENITIC STEEL SINGLE AND POLYCRYSTALS DEFORMED UNDER TENSILE AND IMPACT LOADING

BY

CEMRE OZMENCI

B.Sc., Koc University, 2013

THESIS

Submitted in partial fulfillment of the requirements
for the degree of Master of Science in Mechanical Engineering
in the Graduate School of Sciences
and Engineering of the Koc University, September 2015

Istanbul, Turkey

Koç University

Graduate School of Sciences and Engineering

This is to certify that I have examined this copy of a Master of Science thesis by

Cemre Özmenci

and have found that it is complete and satisfactory in all respects,
and that any and all revisions required by the final
examining committee have been made.

Committee Members:

_____

Demircan Canadinç, Ph.D. (Advisor)

_____

İsmail Lazoğlu, Ph.D.

_____

Nuri Solak, Ph.D.

Date: _____

ABSTRACT

The aim of the work presented herein is to model the roles of micro-deformation mechanisms on the deformation response of high-manganese austenitic steel single and polycrystals deformed under tensile and impact loading. The first part of this study uncovers the individual roles of twinning and slip-twin interactions on the deformation response of twinning induced plasticity steels (TWIP) utilizing a crystal plasticity approach. The plastic deformation mechanisms active in and the strain hardening behaviors of [100], [110] and [216] oriented single crystalline and polycrystalline TWIP samples were investigated at room temperature utilizing combined experimental and numerical methods. Transmission electron microscopy results revealed that very fine twins with a low contribution to the overall twin volume fraction vary in length scales, and interact with each other and dislocations, enhancing the work hardening capacity of the material. In order to predict the corresponding macroscopic deformation response, a novel strain hardening law was proposed, which accounts for the important contributions of slip-twin and grain boundary - dislocation interactions on the strain hardening response. The proposed hardening scheme was implemented into visco-plastic self-consistent crystal plasticity algorithm, and the model successfully predicted the macroscopic deformation response. More importantly, the current findings shed light onto the individual contributions of twinning and slip-twin interactions on the overall work hardening capacity of TWIP steels.

In the second part, a multi-scale modeling approach was applied to predict the impact response of strain rate sensitive high-manganese austenitic steel. The roles of texture, geometry and strain rate sensitivity were successfully taken into account all at once by coupling crystal plasticity and finite element (FE) analysis. Specifically, crystal plasticity was utilized to obtain the multi-axial flow rule at different strain rates based on the experimental

deformation response under uniaxial tensile loading. The equivalent stress – equivalent strain response was then incorporated into the FE model for the sake of a more representative hardening rule under impact loading. The current results demonstrate that reliable predictions can be obtained by proper coupling of crystal plasticity and FE analysis even if the experimental flow rule of the material is acquired under uniaxial loading and at moderate strain rates that are significantly slower than those attained during impact loading. Furthermore, the current findings also demonstrate the need for an experiment-based multi-scale modeling approach for the sake of reliable predictions of the impact response.

ÖZET

Burada sunulan çalışmanın amacı, monoton ve darbe yükleri altındaki tek ve çok kristalli yüksek manganezli östenitik çeliklerin makro-deformasyon davranışlarına etki eden mikro-deformasyon mekanizmalarının rollerinin modellenmesidir. Bu çalışmanın ilk bölümü, Twinning Induced Plasticity (TWIP) çeliklerinde ikizleme ve kayma-ikizleme etkileşimlerinin deformasyon davranışındaki üzerindeki tekil rollerini kristal plastisite yaklaşımıyla açıklamaktadır. [100], [110] ve [216] yönelimli tek kristal ve çok kristalli TWIP çeliği örneklerinin oda sıcaklığındaki plastik deformasyonu ve pekleşme kanunu deneysel ve nümerik metotlar kullanılarak incelenmiştir. Geçirim elektron mikroskop (TEM) sonuçları, toplam ikiz hacim yüzdesine katkısı az olan oldukça ince ikizlerin ölçek olarak değişiklik gösterdiğini, birbirleriyle ve dislokasyonlarla etkileşim halinde olarak malzemenin işlem sertleşme kapasitesini arttırdığını açığa çıkartmıştır. Uygun makroskopik deformasyon davranışını öngörmek için kayma-ikizleme ve dislokasyon-tane sınırı etkileşimlerinin önemli katkılarını içeren özgün bir gerinim sertleşmesi kanunu önerilmiştir. Önerilen pekleşme şeması visko-plastik kendinle uyumlu (VPSC) kristal plastisite algoritmasına dahil edilmiş ve model başarıyla makroskopik deformasyon davranışını öngörmüştür. Daha önemlisi, mevcut bulgular ikizleme ve kayma-ikizleme etkileşimlerinin toplam işlem sertleşme kapasitesi üzerindeki tekil katkılarına ışık tutmuştur.

İkinci bölümde, gerinim duyarlı yüksek manganezli östenitik çeliğin darbe yükü altındaki davranışını öngörmek için çok-ölçekli modelleme yöntemi kullanılmıştır. Kristal plastisite ve sonlu elemanlar (FE) analizi birleştirilerek malzemedeki doku, geometri ve gerinim duyarlılığının rolleri aynı anda dikkate alınmıştır. Spesifik olarak, farklı gerinim hızlarında deneysel tek eksenli çekme yüklemesi verilerine dayalı çok eksenli akma kuralını elde etmek için kristal plastisite kullanılmıştır. Eşdeğer gerilim-eşdeğer gerinim davranışları

darbe yüklemesi altıdaki pekleşme kuralını daha iyi temsil etmek adına FE modeline dâhil edilmiştir. Mevcut bulgular, kristal plastisite ve FE analizlerinin uygun eşleştirilmesi sonucu; malzemenin deneysel akma kuralı darbe yüklemesine oranla dikkate değer düşüklükteki orta dereceli gerinim hızında ve tek eksenli yükeleme altında elde edilse dahi güvenilir sonuçlar verdiğini göstermiştir. Buna ek olarak, mevcut sonuçlar sağlıklı darbe davranışını öngörüsü için deneye dayalı çok ölçekli modelleme yönteminin gerekliliğini kanıtlamıştır.

Dedicated to the best advisor Sir Dr. Demircan Canadinc

and

beloved Advanced Materials Group

ACKNOWLEDGEMENTS

The work presented herein was funded by the Scientific and Technological Research Council of Turkey (TÜBİTAK) under Grant 112M806. Thereby, I want to acknowledge the support of both Koç University and TÜBİTAK.

I would like to thank my friend, brother and advisor Demircan Canadinc for counting me in for the gorgeous mafia group of his. DC's positive energy, endless laughter and -especially- little taps on my suffering left shoulder created the best times in last two years. His superior teachings, guidance, encouragement, support last but not least his cap and sunglasses enabled me to finish this thesis. Beyond my academic study, what is actually far more important is; I made the best friend to dine with and even share my ultimate life goals. He is the best mentor who could ever be and I feel very lucky to have known him.

I would like to thank my committee chair; Dr. Ismail Lazoglu and Dr. Nuri Solak for their valuable advices and participation in my defense jury. I would like to express my deepest appreciation to Dr. Erdem Alaca and Dr. Ersin Yurtsever, for their endless courtesy and support during my Masters study. I also would like to thank Dr. Gregory Gerstein for having us as visiting researchers in Hannover, and sharing his cookies in coffee brakes. I would like to extend my thanks to Dr. Thomas Niendorf, for his valuable contributions and comments. I would also like to thank Dr. Cagatay Basdogan for being such a cheerful office-neighbor.

I am more than grateful to Advanced Materials Group members who become my second family. First of all, I would like to thank Dr. Mine Toker who will always stay as a sister and a mini-advisor in my life. She makes the best horse-jokes of all times and is a powerful congratulations-card guru who just knows what to say or write to make people happy even thousand miles away. I have always enjoyed her company and she taught me that distance is

not important for a true friend. I do not know how to start when it comes to Dr. Burak Bal. He always makes me laugh which is I believe the hardest craft in life. I would like to thank him a lot for his crazy night tours, fun vacation trips and weird advises on relationships. He showed me how to look from different aspects on annoying situations and taught me to be happy and reckless no matter what, utilizing very extraordinary paths. He will always be a dearest friend to me. I would like to thank to Morad Mirzajanzadeh for his friendship and beautiful coffee fortune tellings, hopefully I wrote his last name correctly after two years. He is the first "Babiş" of AMG and my true companion in misfortune. I am very thankful for his unique support and company especially for the hardest last two months of my master's study. I also want to mention my apologies upon destroying his Turkish language abilities and even damaging his native linguistic talent. I would like to thank Benay Uzer, who has this ability of creating awkward situations from dull conversations which usually end up being very funny and unforgettable. She is the hyperactive child of AMG, head of BLS (Bursa Lovers Society) and of course the savior of Tante Helene and adorable Mausy. I would like to thank Dr. Berkay Gumus who always helped AMG with the technical or academic difficulties and office construction issues. He is the person who always suggests effective solutions to various problems and that's why he totally deserves his nickname "emekli". I cannot skip Deniz Aydın and Elmira Sepasi, who became also parts of AMG family. I would like to thank Deniz and Elmira for their friendship and support. Once again I would like to thank Dr. Demircan Canadinc for bringing these lovely people together, being a peacekeeper whenever necessary and never letting anybody out of Advanced Mafia Group.

I would like to thank MIRAY GIZEM YILMAZ who actually threatened me about writing her name in capital letters and encouraged me in the first place for being a mechanical engineer in the sophomore year of our study which created the most necessary condition for this thesis. I deeply appreciate her support, guidance, friendship and her presence in my life. I

would also like to thank Mete Berk Cetiner who stood by me all the time enduring my craziest, most depressed or goofiest moments. Two years of graduate study would be very difficult without his friendship and support. As a very passionate psychologist to be, he helped me more than he is aware of and I feel very lucky to have him as my friend at weekdays. I would like to extend my thanks to Burcu Beykal, Irem Altan, Cansu Cankayali and broticshop members Firat Atalay, Yigit Tunc, Mert Ulku for their friendship and support. I thank Ummu Koc and Mahmut Bicer for being such cheerful neighbors. I would also like to thank Turkan Eryigit, Derya Ernur, Muzaffer Butun, Emine Buyukdurmus, Elif Elmaci, Hacer Abla, Songul Abla and Ayse Abla for their help and support.

Above all, I would like to thank my family for their continuous support and love. I am deeply thankful to my mother Gunes Alsancak, sister DENIZ OZMENCI and brother EFE OZMENCI for the strength they gave me and just being there in my life. I would like to thank my favorite adorable couple Suna and Alkan Alsancak for their endless love and the happiness they create, you two mean a lot to me. I would like to thank my aunt Ates Baran and my uncle Volkan Alsancak again for their absolute support and help.

TABLE OF CONTENTS

LIST OF TABLES

LIST OF FIGURES

1 CHAPTER 1

UNCOVERING THE INDIVIDUAL ROLES OF TWINNING AND SLIP-TWIN INTERACTIONS ON THE DEFORMATION RESPONSE OF TWINNING INDUCED PLASTICITY STEELS: A CRYSTAL PLASTICITY APPROACH

1.1 Introduction

High-manganese austenitic steels (HMnAS) featuring twinning-induced plasticity (TWIP) effect recently attained interest especially from automotive industry [1-6]: high ductility of TWIP steels improve formability of complicated car body components while their outstanding strain hardening capacity makes them good shock absorbers. Having significant strength and toughness, this material allows for manufacturing of light-weight automobile parts without sacrificing from safety, thereby further improving the carbon emission performance of the vehicles [1–6]. In order to broaden the scope of the utility of this class of steels, tailoring their mechanical properties and performance, and fully understanding the underlying reasons of their remarkable work hardening is imperative. With this motivation, numerous studies have been carried out, however; despite a decade-long accumulation of knowledge, relative contributions of active deformation mechanisms to the overall work hardening of TWIP steel have not been clearly laid out yet.

TWIP steels have a stable face-centered cubic (FCC) structure with a chemical composition of Fe, 25-35 wt.% Mn, less than 1 wt.% C, and other minor alloying elements, such as Al, V, Cr and Si. This class of advanced steels characteristically have a low stacking fault energy (SFE) ranging from 20 to 40 mJ m^{-2}, which allows for simultaneous slip and twinning activity starting in the early stages of plastic deformation at room temperature [7–11]. As for the outstanding work hardening capacity of HMnAS, including TWIP steels, two different reasons stand out: dynamic strain aging and the dynamic Hall-Petch effect [12-23].

In the case of dynamic strain aging (DSA), mobile carbon (C) atoms couple with manganese (Mn) atoms throughout the lattice. These C-Mn couples reorient in the cores of dislocations and create ubiquitous small stress localizations during plastic deformation, which delays necking [12–17]. DSA is an important phenomenon for HMnAS exhibiting serrated flow [15,16,18], however; the observed mechanical response of TWIP steels cannot be attributed to DSA only, since multiple competitive micro-deformation mechanisms are simultaneously active [1,13,14], where the effect of twinning is especially incontrovertible. As for the so-called dynamic Hall-Petch effect, mechanical twins divide initial grains into sub-grains as the deformation proceeds. Consequently, even though they are relatively less impenetrable [11,19–23], the twin boundaries constitute additional barriers that prevent dislocation motion as the grain boundaries do [24,25]. Indeed, the debate on whether DSA or dynamic Hall-Petch dictates the hardening behavior of TWIP steels has been the subject of several works [13-19], and it has been demonstrated that TWIP steels with minor DSA activity still exhibit high work hardening rates [17] while the DSA effect remains rather limited in HMnAS with carbon content less than 0.6 wt% in the presence of significant twinning activity [14]. Accordingly current study focuses on revealing the effect of mechanical twins on work hardening of TWIP steels rather than the effect of DSA.

One of the first experimental investigations on the role of twinning on the mechanical behavior of HMnAS was forwarded by Remy et al. [19], who suggested that mechanical twins act as strong obstacles that prevent dislocation glide, eventually leading to the high work hardening rate exhibited by HMnAS. Following Remy et al., slip-twin interactions were associated with the high work hardening rates exhibited by TWIP steels [26], such that twins provide effective barriers that reduce the mean free path (MFP) of glide dislocations [6,26]. Formation of nano-twins within primary twins were demonstrated to further promote strain hardening in TWIP steels [25,27–29].

Further experimental studies revealed that a significant fraction of twins are in the order of nanometers, especially during the early stages of deformation [30,31]. For instance, Idrissi et al. [32] presented experimental evidence for slip-twin interactions utilizing detailed in-situ transmission electron microscopy (TEM). However, examined area in a typical TEM sample is very limited and the obtained information is two dimensional, reflecting only the deformed surface but not the bulk texture. Thus, different methods have been employed to enlarge the inspected area as compared to a standard TEM sample: for instance, Steinmetz et al. [11] used electron channeling contrast imaging (ECCI) on TWIP steel, and with the based on the corresponding experimental observations, proposed a constitutive model to simulate work hardening of TWIP steel, incorporating twin nucleation, slip-twin interactions, twin growth and temperature effect without considering any grain orientation or reorientation [11]. However, despite the considerably larger examination area of a typical ECCI sample, this technique was not able to detect the nano-twin structures that formed in the early stages of deformation due to inadequate resolution and scale difference. Moreover, nano-twins forming in the early stages of deformation evolve to macro-twins with proceeding deformation, which become visible through even confocal microscopy during later stages of the deformation, but therefore are too large to be properly investigated under TEM [28]. Accordingly, the influence of mechanical twinning on the deformation response becomes more evident concomitant with increasing deformation rate, however; in-situ and post-experimental electron-optical techniques have so far proven insufficient for drawing solid conclusions on individual contributions of slip and twinning due to scale variation of twins throughout the complete plastic deformation regime.

To overcome this scale transition difficulty, various studies adopted combined experimental-numerical techniques, or fully theoretical models to understand the role of twinning in TWIP steels [5,7,24,33,34]. Allain et al. [24] developed a constitutive law for

predicting the evolution of twin volume fraction of TWIP steels, and mathematically formulated the thickening of hundred-nanometer-wide micro-twin stacks into a few tens of micrometers. A different approach, where a self-consistent elastic-viscoplastic crystal plasticity approach based on homogenization of representative volume elements was utilized, theoretically demonstrated that the slip-twin interactions dictate the work hardening response in TWIP steels following about 15% strain [34]. In addition, Dancette et al. [33] investigated hardening behavior and texture development of polycrystalline TWIP steels making use of crystal plasticity-based finite element method (CPFEM) [35–37] and statistical Taylor-type homogenization-based multisite advanced Lamel (ALAMEL) [38] method. The ALAMEL model proved successful for early stages of plastic deformation, while CPFEM approach provided more accurate predictions in the later stages of deformation, and thus, neither model was sufficient in predicting the complete deformation response [33].

In order to successfully predict the macroscopic response behavior of TWIP steels throughout the entire range of deformation and by accounting for their microscopic deformation mechanisms and textures, the well-known visco-plastic self-consistent (VPSC) crystal plasticity algorithm [39,40] developed by Lebensohn and Tome was utilized by several researchers [5,7]. For instance, Prakash et al. [5] utilized the predominant twin reorientation (PTR) method [41] adopted in VPSC to predict the twinning activity and texture evolution in TWIP steels, and compared this approach to that proposed by Kalidindi et al. [42,43]. In the PTR method, number of grains in the polycrystalline aggregate does not change, however; each grain is reoriented when the twinning volume fraction exceeds a threshold value. In Kalidindi's model, on the other hand, subdivision of grains by twinning is allowed for, and only the twinned region is reoriented rather than the whole grain. It was concluded that PTR is a better method to predict TWIP steel deformation response. Supporting evidence was forwarded by Saleh et al. [7] who investigated three different micro-deformation models

utilizing VPSC: activation of only partial slip, PTR method, and twinning treated as directional slip. A comparison of these three models also revealed that the PTR method provided the best predictions of mechanical response and texture evolution, as evidenced by experimental deformation, XRD and EBSD results.

VPSC was previously utilized with great success for clarifying the contributions of different micro-deformation mechanisms to the exceptional work hardening response of Hadfield steel, which constitutes the basis of many HMnAS, including TWIP steels. For instance, in the works of Karaman et al.[44–47] on both single and polycrystals of Hadfield steels, the classical Voce hardening formulation was improved by introducing additional terms that accounted for the contribution to hardening imposed by the hindering of dislocation motion by twin and grain boundaries [47], such that an ultrafine-grained structure was mimicked. Likewise, Canadinc et al [10,48] modeled the role of high-density dislocation walls (HDDWs) on the hardening response of Hadfield steel with VPSC. Specifically, the three-dimensional geometry-based interaction between the glide dislocations and the HDDWs was incorporated into the classical Voce hardening scheme as an additional flow stress rate.

Following the approach proposed by Canadinc et al., present work focuses on identifying and modeling the individual and collective roles of active micro-deformation mechanisms on the strain hardening response of TWIP steels. Specifically, the influences of slip, twinning, slip-grain boundary and slip-twin interactions on the deformation response of single- and polycrystalline TWIP steels were studied within the VPSC crystal plasticity framework. A physics-based constitutive law was proposed and incorporated into VPSC model to geometrically account for twin-slip interactions, where twins were modeled as effective barriers against dislocation motion. A comparison of experimental results and numerical simulations revealed that mechanical twins significantly contribute to the rapid strain hardening of TWIP steel. Secondary twinning is especially allowed in VPSC

simulations to simulate nano-twin formation within twinned regions which is experimentally observed to be an important mechanism responsible for the superior ductility of this material [27]. The combined numerical and experimental approach presented herein not only demonstrates the success of the proposed constitutive law in predicting the experimental deformation response and the corresponding work hardening throughout the whole plastic regime, but also uncovers the individual contribution of scale-variant twinning activity to the overall work hardening in TWIP steels. Moreover, the current findings on the physics of twinning in TWIP steels constitute a step forward in understanding the complicated micro-deformation mechanisms active in TWIP steels, and open a new venue for improving the manufacturing quality and performance of new generation advanced steel grades.

1.2 Experimental Procedures

The material investigated in this work is the commercial X-IP^{TM} 1000 TWIP steel (0.6 C, 22.36 Mn, 0.25 V, 0.2 Cr, 0.25 Si wt.%) with a sheet thickness of 1.6mm and an average grain size of about 2μm. For single crystal growth, the Bridgman technique with a Helium atmosphere was employed. The chemical composition of the single crystal was determined to be very similar with a slight decrease in the Mn content from 22.36 to 21.7 wt. %. Samples featuring a gauge section with the dimensions of 15mm × 3mm × 1.6mm were machined from the initilal polycrystalline sheet and the single crystals by electro-discharge machining (EDM). In order to remove the EDM-affected surface layer and to ensure a high surface quality, all samples were mechanically ground down to a grit size of 5μm prior to testing.

1.3 Incorporation of slip-twin and slip-grain boundary misorientation angle interactions into VPSC algorithm

In present work, the total hardening is attributed to three main components: the first component accounts for the hardening due to dislocation motion in grains, second due to dislocation motion – twin interactions and third due to dislocation motion – grain boundary interactions. The overall dislocation density can be expressed as

$$\dot{\rho} = \sum_n \{k_1\sqrt{\rho} - k_2\rho\}|\dot{\gamma}^n| + \sum_n \sum_r \frac{K}{cb}\cos\theta_{nr}|\dot{\gamma}^n| + \sum_n \sum_q \frac{K}{db}(1+\sin\theta_q)|\dot{\gamma}^n| \quad (1)$$

where k_1 and k_2 are constants, K is a geometric constant, and b represents the burger vector.The term c represents the average spacing between twins. The term $\sum_n \sum_r \frac{K}{cb}\cos\theta_{nr}|\dot{\gamma}^n|$ accounts for the contribution due to the interaction between the dislocations on the active slip system n and the active twin system r. The angle θ_{nr} is the angle between the plane normals of the active slip and twinning systems (Figure 1.3.1). The third term $\sum_n \sum_q \frac{K}{db}(1+\sin\theta_q)|\dot{\gamma}^n|$ accounts for the contribution due to the interaction between the dislocations on the active slip system n in grain one and the grain boundary of the neighboring grain two [49,50]. The term d represents the average grain size of the aggregate. The angle θ_q is the misorientation angle between the surface normals of grains one and two (Figure 1.3.2).

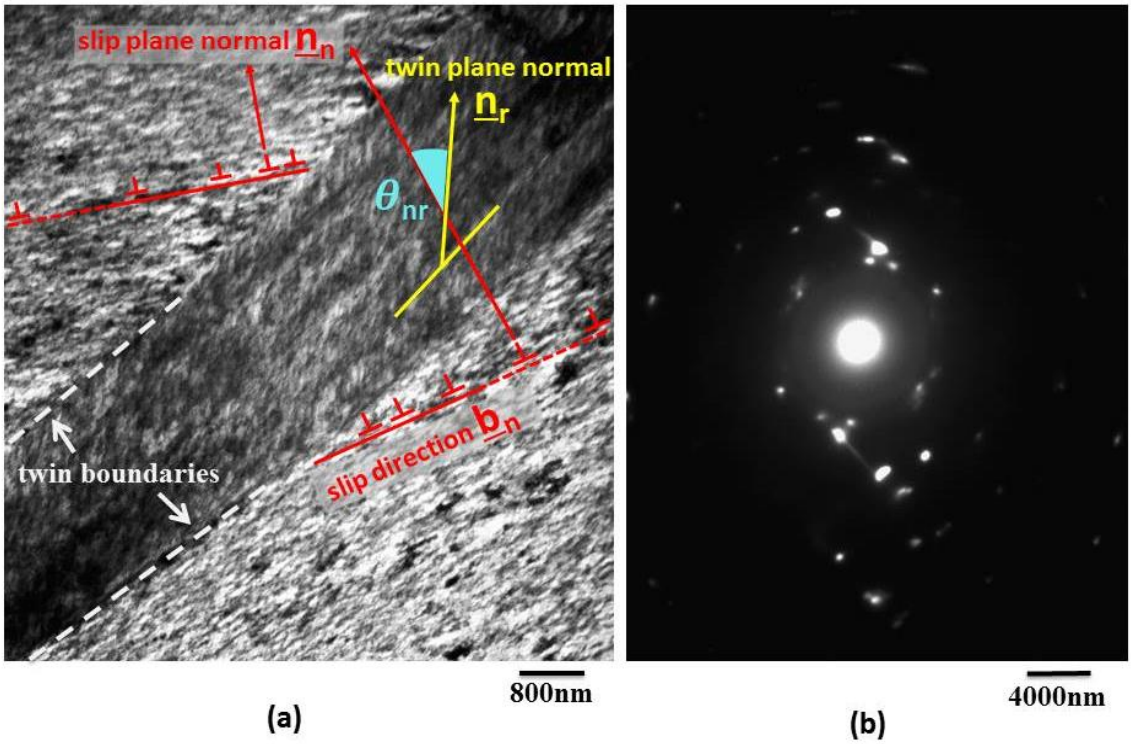

Figure 1.3.1. (a) Schematic representation of the interaction between twin system r and active slip system n, (b) selected area diffraction (SAD) pattern evidencing twinning activity.

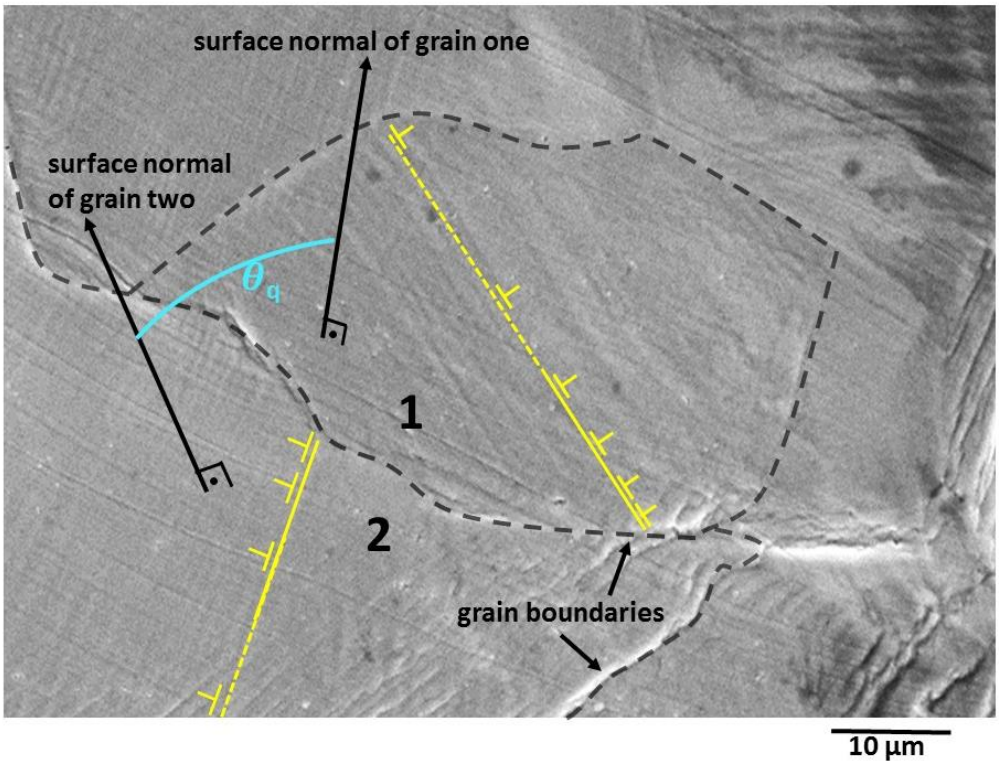

Figure 1.3.2. Schematic representation of the interaction between grain boundary misorientation angles and active slip system n.

We define the flow stress τ in the traditional Taylor hardening format as

$$\tau - \tau_0 = \alpha\mu b\sqrt{\rho} \tag{2}$$

where τ_0 is a reference strength, which is taken as the microscopic yield in our analysis. The relationship between the term c, average spacing between twins and the term f, representing the volume fraction of twinning in grain, is defined as follows:

$$\frac{1}{c} = \frac{1}{2t}\frac{f}{1-f} \tag{3}$$

where t represents the average twinned region thickness which is taken as 10^{-7} m [8]. The time derivative of Eq. (2) in which τ_0 is taken as constant, gives the rate of flow stress as follows:

$$\dot{\tau} = \frac{\alpha\mu b\dot{\rho}}{2\sqrt{\rho}} \tag{4}$$

Substituting Eq. (1) into Eq. (4) results in

$$\dot{\tau} = \frac{\alpha\mu b}{2\sqrt{\rho}}\sum_n\left\{\frac{K}{cb}\sum_r \cos\theta_{nr} + \frac{K}{db}\sum_q\left(1+\sin\theta_q\right) + k_1\sqrt{\rho} - k_2\rho\right\}|\dot{\gamma}^n| \tag{5}$$

which simplifies to

$$\dot{\tau} = \sum_n\left\{\frac{\alpha\mu K}{2c\sqrt{\rho}}\sum_r \cos\theta_{nr} + \frac{\alpha\mu K}{2d\sqrt{\rho}}\sum_q\left(1+\sin\theta_q\right) + k_1\frac{\alpha\mu b}{2} - k_2\frac{\alpha\mu b}{2}\sqrt{\rho}\right\}|\dot{\gamma}^n| \tag{6}$$

From Eq. (2), the following identity is obtained for the square root of the density of dislocations:

$$\sqrt{\rho} = \frac{\tau-\tau_0}{\alpha\mu b} \tag{7}$$

Once the Eqs. (3) and (7) are substituted into Eq. (6), the rate of flow stress evolution is given by

$$\dot{\tau} = \sum_n\left[\frac{\alpha^2\mu^2 bK}{4t(\tau-\tau_0)}\frac{f}{1-f}\sum_r \cos\theta_{nr} + \frac{\alpha^2\mu^2 bK}{2d(\tau-\tau_0)}\sum_q\left(1+\sin\theta_q\right) + \left\{k_1\frac{\alpha\mu b}{2} - k_2\frac{(\tau-\tau_0)}{2}\right\}\right]|\dot{\gamma}^n| \tag{8}$$

One should note that the term $\left\{k_1\frac{\alpha\mu b}{2} - k_2\frac{(\tau-\tau_0)}{2}\right\}$ in Eq. (8) is the well-known Voce hardening term. Eq. (8) can also be written as [51,52]:

$$\dot{\tau} = \sum_n \left[\frac{\alpha^2\mu^2 bK}{4t(\tau-\tau_0)}\frac{f}{1-f}\sum_r \cos\theta_{nr} + \frac{\alpha^2\mu^2 bK}{2d(\tau-\tau_0)}\sum_q\left(1+\sin\theta_q\right) + \left\{\theta_0\left(\frac{\tau_s-\tau}{\tau_s-\tau_0}\right)\right\}\right]|\dot{\gamma}^n| \quad (9)$$

where $\theta_0$and τ_s are constant strain hardening rate and the saturation stress in the absence of geometric effects, or the threshold stress respectively. Eq. (9) represents the full hardening law which considers twin-slip and slip-grain boundary interactions of TWIP steel. $\left\{\theta_0\left(\frac{\tau_s-\tau}{\tau_s-\tau_0}\right)\right\}$ term in eq. 9 is the classical Voce hardening term. VPSC algorithm utilizes a reference hardening function for each micro deformation system which is the extended version of the classical Voce hardening term [51,53] defined as below:

$$\tau^s = \tau_0 + (\tau_1 + \theta_1\Gamma)\left(1 - exp\left(-\frac{\theta_0\Gamma}{\tau_1}\right)\right) \quad (10)$$

where τ_0 is the initial critical resolved shear stress (CRSS). Hardening is defined in eq. 10 by the parameters, θ_0, θ_1 and $(\tau_0+\tau_1)$ which are initial hardening rate, the asymptotic hardening rate and the back-extrapolated CRSS respectively [54]. Hardening parameters of the poly-crystal and single crystal samples of TWIP steel are provided in Figures 1.4.1-1.4.4. Table 1.3.1 shows the numerical values of constants [27,44,55] that are used in eq. 9 which is the full hardening law.

Table 1.3.1. Constants used in eq. (9) for poly-crystal and single crystals oriented along [100], [110] and [216].

Constants	**μ (MPa)**	**α**	**$\underline{b}$**	***K***	***t* (m)**	***d* (m)**
Numerical value	**71×10^3**	**0.4**	**2.58×10^{-10}**	**8×10^4**	**10^{-7}**	**20×10^{-6}**

1.4 Results & Discussion

The room temperature experimental and simulated tensile true stess - true inelastic strain responses of [100], [110] and [216] oriented single crystalline, and polycrystalline X-IP TWIP steel samples are provided in figures 1.4.1-1.4.4. All single crystalline samples experimentally displayed high ductility with minimum 70% true inelastic strain concomitant with high strength, attaining a minimum of 900 MPa true stress, indicating the rapid hardening characteristically observed in TWIP steels. Polycrystalline samples, on the other hand, exhibited 45% true inelastic strain with a superior strength of about1600 MPa. The stress-strain responses of X-IP steel samples were predicted by first applying the original VPSC model, and then by utilizing the modified VPSC algorithm which takes the slip-twinning and dislocation-slip interactions into account as explained in eqs. 1-10.

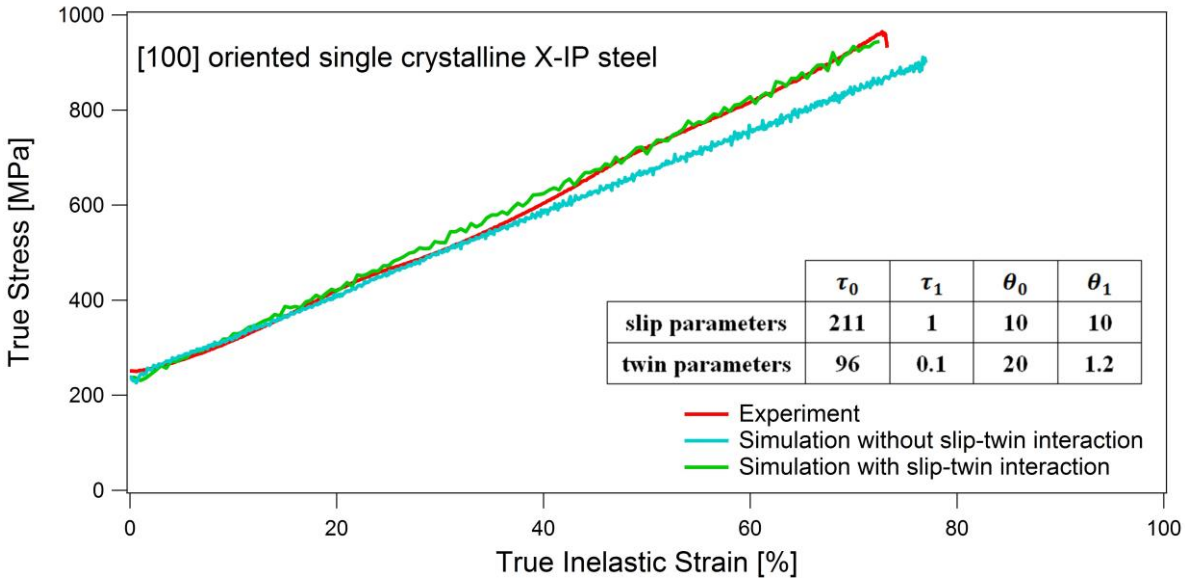

Figure 1.4.1. Experimental uniaxial tensile deformation response of the [100] oriented single crystalline X-IP steel samples and the corresponding crystal plasticity simulations. The Voce hardening parameters for the simulation accounting for the slip-twin interactions are provided in the inset.

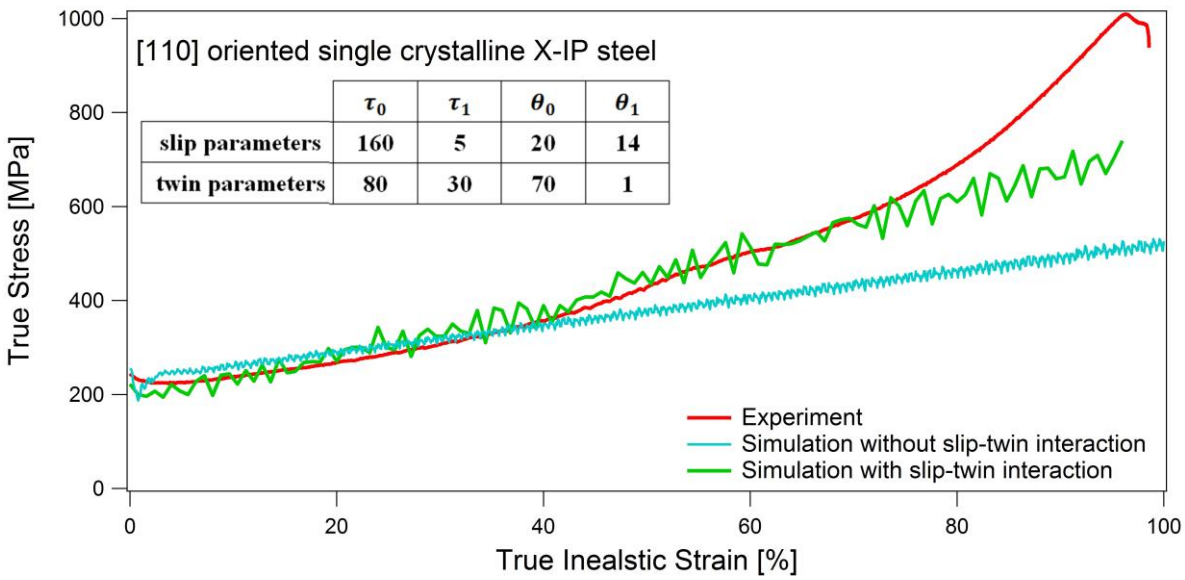

Figure 1.4.2. Experimental uniaxial tensile deformation response of the [110] oriented single crystalline X-IP steel samples and the corresponding crystal plasticity simulations. The Voce hardening parameters for the simulation accounting for the slip-twin interactions are provided in the inset.

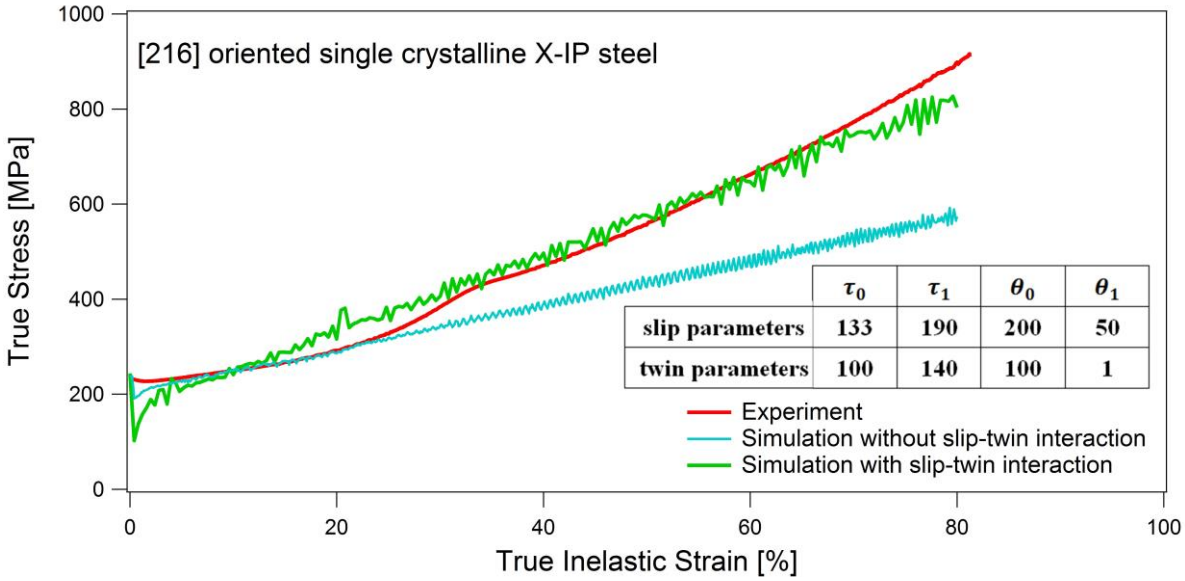

Figure 1.4.3. Experimental uniaxial tensile deformation response of the [216] oriented single crystalline X-IP steel samples and the corresponding crystal plasticity simulations. The Voce hardening parameters for the simulation accounting for the slip-twin interactions are provided in the inset.

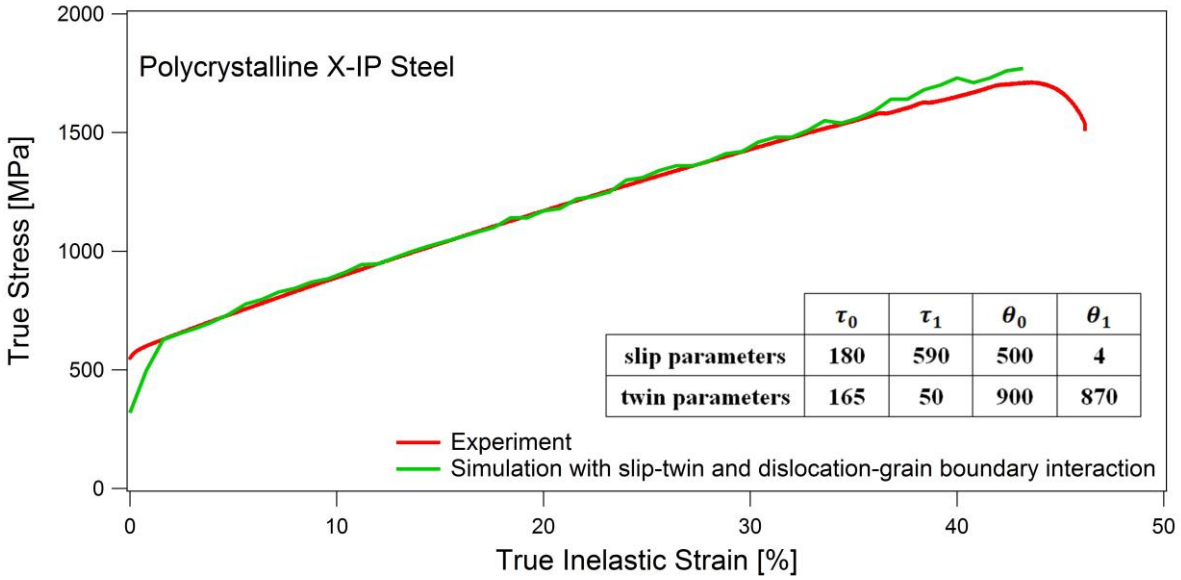

	τ_0	τ_1	θ_0	θ_1
slip parameters	180	590	500	4
twin parameters	165	50	900	870

Figure 1.4.4. Experimental uniaxial tensile deformation response of polycrystalline X-IP steel samples and the corresponding crystal plasticity simulations. The Voce hardening parameters for the simulation accounting for the slip-twin interactions are provided in the inset.

In Figures 1.4.1-1.4.4., the elastic portions of the experimental tensile deformation data are excluded from the true inelastic stress-strain curves since the VPSC model only considers the plastic deformation of the polycrystalline materials. For single crystal modeling, the same Euler angles, which were determined by experimental XRD analyses, were assigned to all grains such that the overall aggregate has the corresponding single crystalline sample texture. As for the polycrystalline samples, the experimentally measured texture was utilized as a direct input for VPSC. Accounting full anisotropy; <110> (111) primary slip, <110> (112) primary twinning and <110> (112) secondary twinning systems are activated while modeling X-IP TWIP steels. Secondary twinning system which allows further twinning in already twinned regions is allowed since this material exhibits secondary micro-twins or even nano-twins within existed twins instead of twin thickening (Figures 1.4.5 and 1.4.6) [27–30,56,57]. Although classical Voce hardening law already defined within original VPSC algorithm [51,54] simulated the [100] oriented single crystal X-IP steel's plastic deformation behavior well (figure 1.4.1, simulation without slip-twin interaction); the hardening of [110] and [216]

oriented single crystals are under predicted, especially beyond plastic strains of 40% and 30%, respectively (figures 1.4.2 and 1.4.3, simulation without slip-twin interaction).

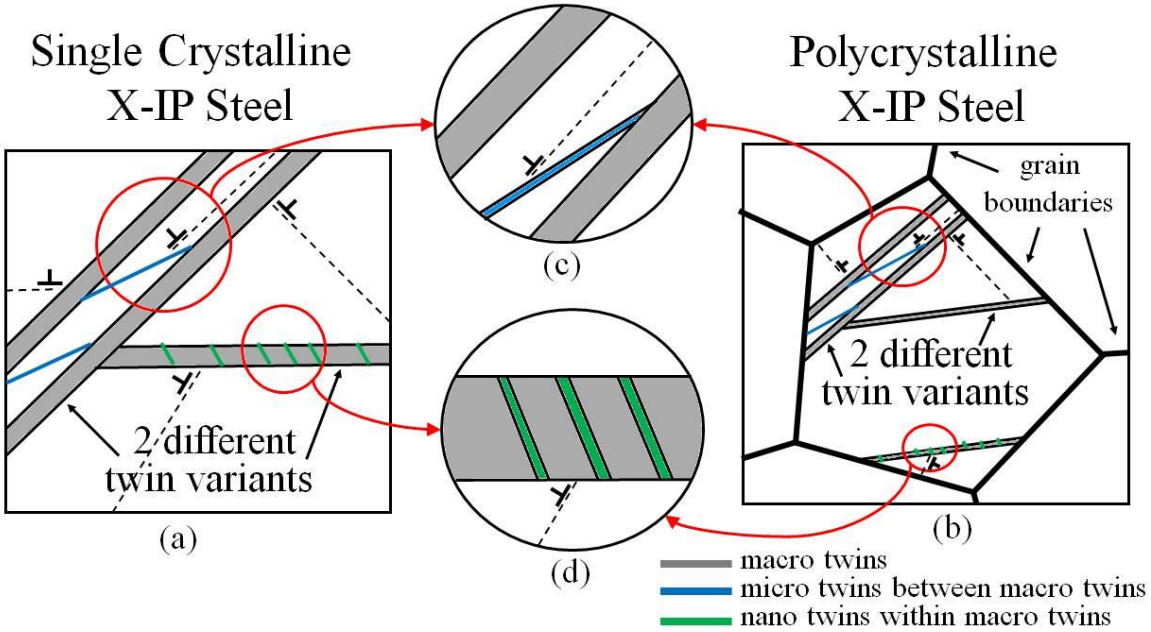

Figure 1.4.5. Schematic representation of scale-variant twinning activity, and dislocation-twin and dislocation - grain boundary interactions in single- and polycrystalline X-IP steel samples.

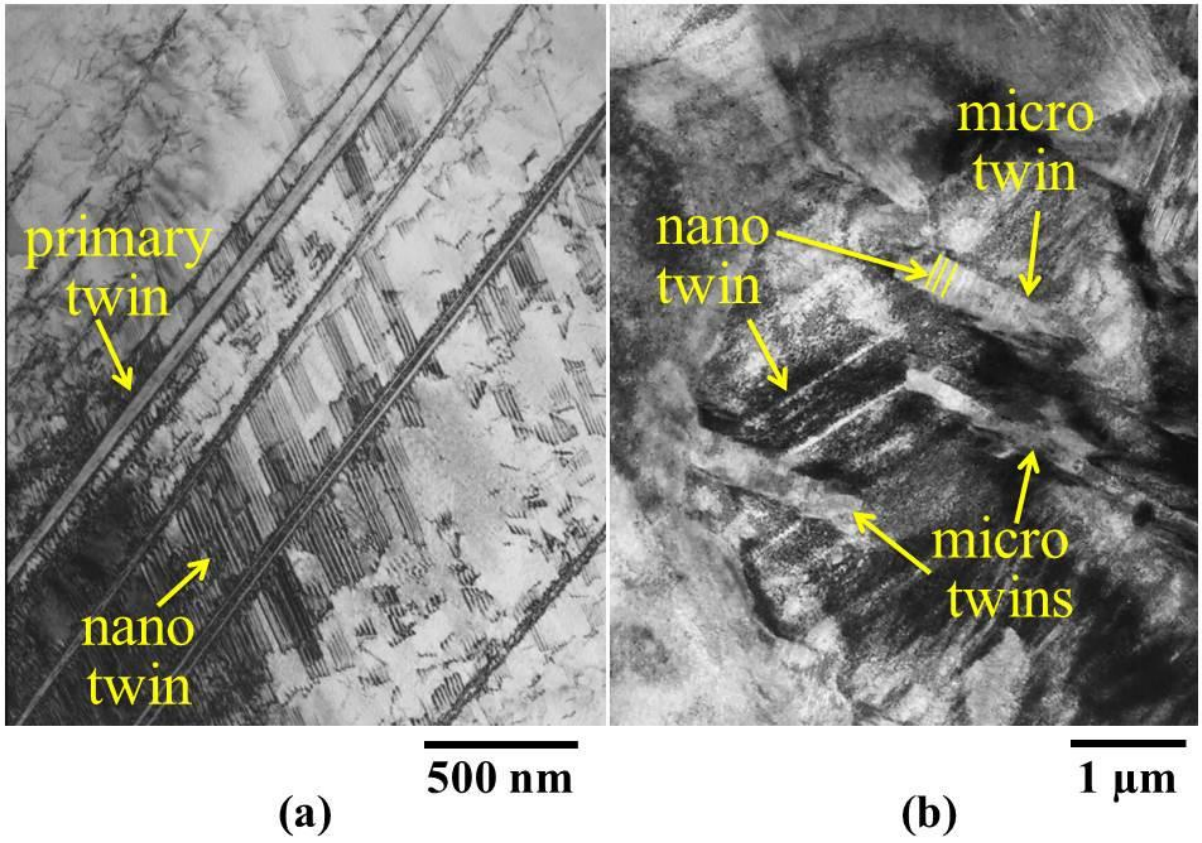

Figure 1.4.6. TEM images of (a) [216] oriented single crystalline X-IP steel exhibiting two

different nano-twin variants as schematically shown in figure 1.4.5 c, and (b) polycrystalline X-IP steel exhibiting micro- and nano-twin interactions as schematically shown in figures 1.4.5 c and 1.4.5 d. Both TEM images were recorded upon failure of the samples.

Hence, hardening law of the TWIP steel is re-defined by implementing twin-slip and dislocation-grain boundary interactions into VPSC algorithm explained in previous chapter in eqs. 1-10. Voce hardening parameters that are used for fitting are provided as insets in figures 1.4.1-1.4.4. The parameter τ_0 which defines the critical shear stress for slip motion ($CRSS_s$) is calculated according to Schmid's law [58] for the single crystal cases. For the poly crystalline sample, $CRSS_s$ was determined by dividing the corresponding experimental yield value by the Taylor Factor [59]. For the critical resolve shear stress considering twinning mechanism ($CRSS_t$), there are multiple theories proposed in literature [11,24,44,57,60], however; none of these models have been successful in explaining or predicting the experimentally observed deformation behavior of TWIP steels, yet. It is well-known that grain boundaries act as twin nucleation sources in polycrystals [2,60], however; for the single crystals pre-existing defects, Lomer-Cottrell locks, pre-existing dislocations that evolve into multi-layered stacking faults, or intrinsic stacking faults are usually thought to be the sources of twinning [44–47,60–63]. Although twin nucleation mechanism is beyond the scope of the current study, closely related microscopic yield stress of twinning becomes important for VPSC simulations. A significant number of studies argued that multiple slip systems should be active to initiate twinning [2,44,61,64,65]. On the other hand, Karaman et. al. reported having a higher Schmid factor, twinning is the primary microscopic deformation system and twinning initiates before slip in [111] oriented single crystalline Hadfield steel [45]. Recently, supporting Karaman et. al. [45] Rahman et. al. conducted a cyclic loading test on polycrystalline TWIP steel at stresses 200 MPa which is much below the macroscopic yield stress and observed plastic deformation [56,57]. Developed plastic deformation at low stresses is attributed to occurrence of nano-twins that diffracted intensity and peak width profiles revealed besides TEM images. It was

concluded that twinning is related to the partial dislocations yet starts prior to slip motion [56,57]. In this study; $CRSS_t$ is treated as a Voce hardening parameter and the best result is obtained only if $CRSS_t$ is defined lower than the $CRSS_s$ as can be seen in figures 1.4.1-1.4.4. This result supports that twinning mechanism becomes active earlier than dislocation slip in TWIP steels.

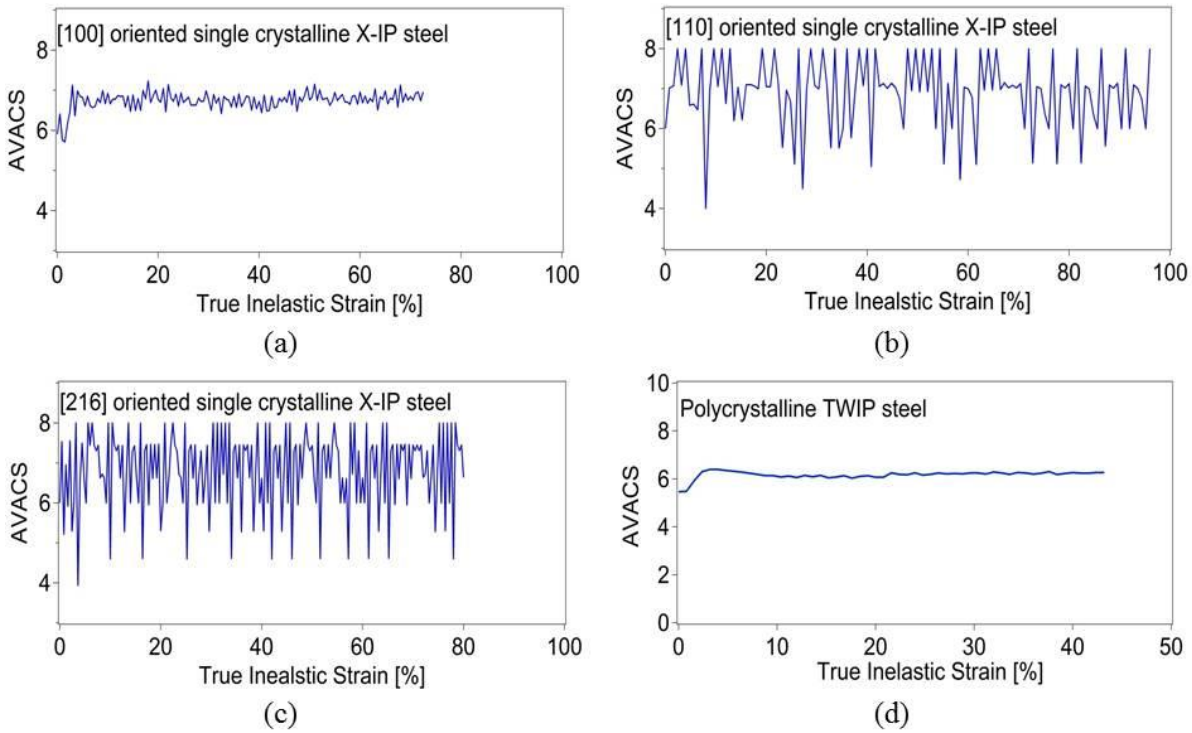

Figure 1.4.7. Average number of active systems (AVACS) predicted by VPSC accounting for slip-twin interactions throughout the deformation of (a) [100], (b) [110], (c) [216] oriented single crystal and (d) polycrystalline X-IP steels.

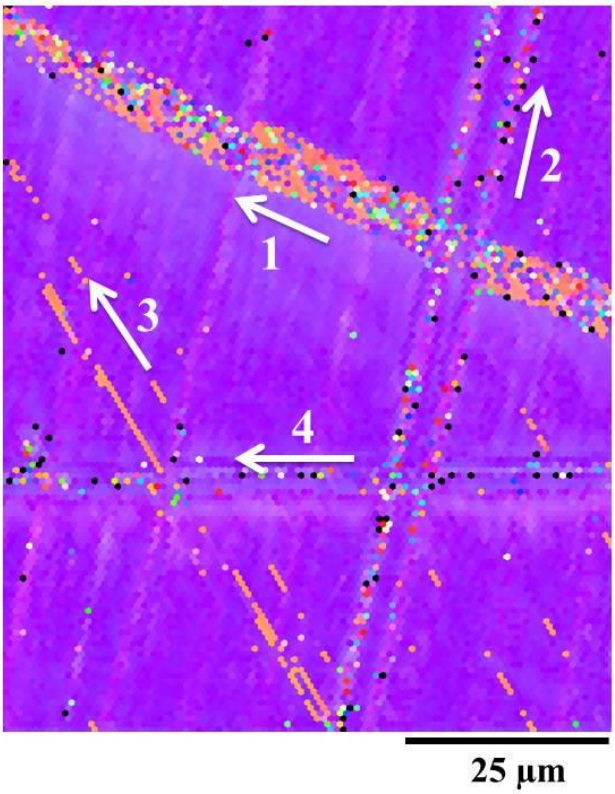

Figure 1.4.8. EBSD image of [110] oriented single crystalline X-IP steel sample deformed to 35% strain showing only four different active deformation systems.

Introduced VPSC simulations validates not only the strong effect of dislocation pile-ups trapped in twin boundaries on macroscopic response of the TWIP steel, but also accounts for nano and micro twin formations. For [110] oriented single crystal X-IP steel, only four active systems are visible via electron backscatter diffraction (figure 1.4.8) however VPSC simulations with slip-twin interaction shows that on average, seven different systems are active. Since micro and nano twins that form within macro twins [28–30,56] are only visible via TEM because of the scale variance and since the spatial resolution of EBSD is insufficient to capture that small orientation difference. Accordingly, such difference between EBSD results and VPSC simulations with slip-twin interaction was expected. Utilized numerical approach was able to capture the average number of active systems (AVACS) throughout the plastic deformation in a more realistic way than EBSD or ECCI.

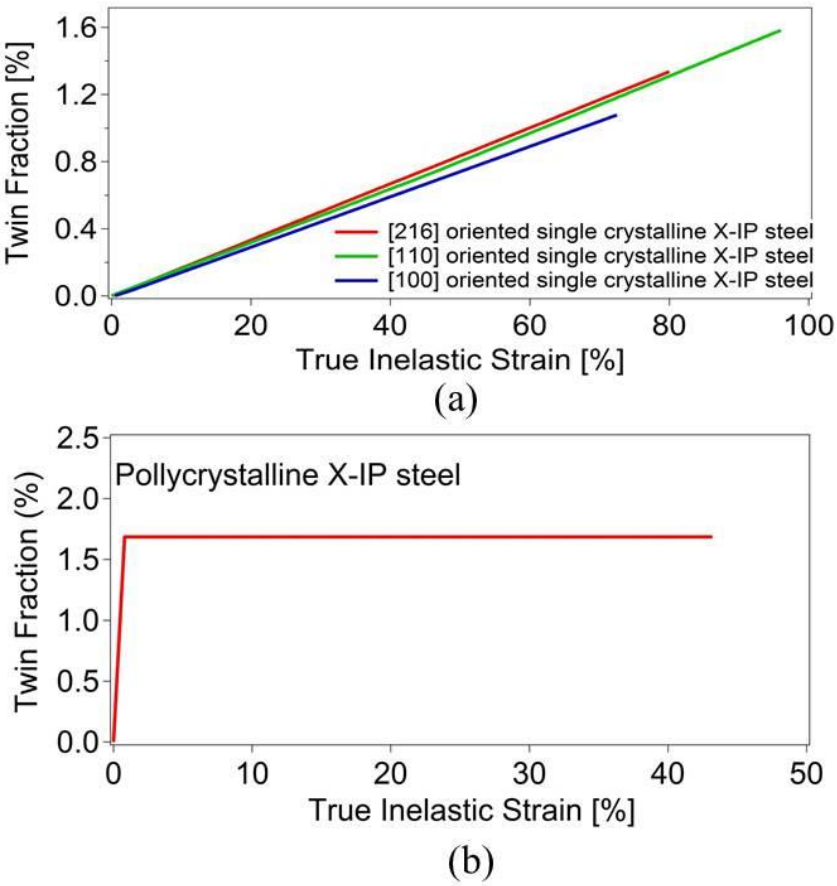

Figure 1.4.9. Total twin fraction predicted by VPSC simulations with slip-twin interaction in (a) single crystalline and with slip-twin and dislocation-grain boundary interactions in (b) polycrystalline X-IP steels.

Studies on texture evolution of TWIP steel revealed that twins are very thin and do not have enough volume to affect the texture however have strong influence in hardening [2,28,30,31]. De Cooman et. al. [30] utilized the original VPSC algorithm to model twin fraction of polycrystalline TWIP steels and reported 10% twin volume fraction at 0.45 true strain: even though twin volume effect is rather large in VPSC simulations, the experimental inverse pole figures of TWIP steels conversely show very small fraction of few twins with nanometer-thickness on fracture surface, which cannot significantly contribute to the overall twinning volume fraction [30]. Similarly, Yan et. al. [31] used the original VPSC algorithm while modeling polycrystalline TWIP steels neglecting the interactions between twin and slip mechanisms, and reported that contribution of twinning is over-predicted compared to

experimental results and twin volume fracture is indicated as 10% by VPSC at 47% plastic strain. It was concluded that twinning and slip alternates during plastic deformation [31] which is consistent with figure 1.4.7. In this study utilizing the same algorithm with re-defined hardening law, twin volume fraction is determined as less than 2% for single and poly crystal TWIP samples.

Figures 1.4.1-1.4.9 show the success of the proposed constitutive law in predicting the experimental deformation response with corresponding work hardening and individual roles of twinning and slip throughout the whole plastic regime. Specifically, the current findings reveal that scale-variant twinning activity provides grain boundary-like obstacles against dislocation slip, and thereby trap dislocations (Figures 1.4.5 and 1.4.6).Even though the simulated twin volume fraction was very low (about 1.5%), VPSC results show that slip-twin interactions highly contribute to hardening of the TWIP steel which is coherent with the experimental findings in literature [2,27,29–31,56,57]. High number of active deformation systems and low twin volume fraction reveal the importance of scale-variant twining activity on the macroscopic deformation response of TWIP steel. It should be noted that, even though the current modified VPSC model is able to capture the effects of all active systems on the overall deformation response, including nano-scale twins, the average twin thickness was introduced as 100nm [27] in the algorithm for all possible twin systems (Table 1.3.1). Attaining varying thicknesses for different twin systems and predicting discrete twin volume fractions at different scales is left for future work, since the currently available experimental techniques are limited to a very small volume of the material, significantly restricting a reliable assessment of the respective volume fractions of the involved micro- and nano-deformation mechanisms.

1.5 Conclusions

The present study was undertaken with the motivation of establishing the individual roles of twinning and slip-twin interactions, as well as the dislocation - grain boundary interactions, on the deformation response of twinning-induced plasticity (TWIP) steels. For this purpose, utilizing combined experimental and numerical methods, [100], [110] and [216] oriented single crystalline, and polycrystalline samples of the commercially available X-IP TWIP steel were investigated. The following conclusions can be drawn from the work presented herein:

- A visco-plastic self-consistent (VPSC) crystal plasticity model was modified to model the uniaxial tensile deformation response of the X-IP TWIP steel samples. The proposed hardening law which accounts for slip-twin interactions, as well as dislocation - grain boundary interactions, yielded successful predictions of the macroscopic deformation response.

- The current findings support the argument that twinning initiates before slip in TWIP steels. Specifically, the critical resolved shear stress (CRSS) for twinning is lower than the CRSS for slip. Furthermore, experimental evidence shows that nano-twins forming within primary twins actively contribute to the load bearing capacity and the overall work hardening of the X-IP steel single- and polycrystalline samples at room temperature.

- Very fine twins with a total volume fraction of 1.5% form in varying length scales in TWIP steels throughout deformation. Even though twin volume fraction is very low, slip-twin interactions highly contribute to overall hardening capacity since twins constitute strong obstacles against dislocation motion. At the same time, formation of nano-scale twins within

primary twins provides a venue for the continuation of plastic deformation, increasing both the ductility and the load bearing capacity of X-IP TWIP steels.

1.6 References

[1] O. Bouaziz, S. Allain, C.P. Scott, P. Cugy, D. Barbier, High manganese austenitic twinning induced plasticity steels: A review of the microstructure properties relationships, Curr. Opin. Solid State Mater. Sci. 15 (2011) 141–168. doi:10.1016/j.cossms.2011.04.002.

[2] H. Beladi, I.B. Timokhina, Y. Estrin, J. Kim, B.C. De Cooman, S.K. Kim, Orientation dependence of twinning and strain hardening behaviour of a high manganese twinning induced plasticity steel with polycrystalline structure, Acta Mater. 59 (2011) 7787–7799. doi:10.1016/j.actamat.2011.08.031.

[3] T. Niendorf, F. Rubitschek, H.J. Maier, J. Niendorf, H. a. Richard, a. Frehn, Fatigue crack growth-Microstructure relationships in a high-manganese austenitic TWIP steel, Mater. Sci. Eng. A. 527 (2010) 2412–2417. doi:10.1016/j.msea.2009.12.012.

[4] T. Niendorf, C. Lotze, D. Canadinc, a. Frehn, H.J. Maier, The role of monotonic pre-deformation on the fatigue performance of a high-manganese austenitic TWIP steel, Mater. Sci. Eng. A. 499 (2009) 518–524. doi:10.1016/j.msea.2008.09.033.

[5] A. Prakash, T. Hochrainer, E. Reisacher, H. Riedel, Twinning Models in Self-Consistent Texture Simulations of TWIP Steels, Steel Res. Int. 79 (2008) 645–652. doi:10.2374/SRI08SP030-79-2008-645.

[6] O. Bouaziz, S. Allain, C. Scott, Effect of grain and twin boundaries on the hardening mechanisms of twinning-induced plasticity steels, Scr. Mater. 58 (2008) 484–487. doi:10.1016/j.scriptamat.2007.10.050.

[7] A. a. Saleh, E. V. Pereloma, A. a. Gazder, Microstructure and texture evolution in a twinning-induced-plasticity steel during uniaxial tension, Acta Mater. 61 (2013) 2671–2691. doi:10.1016/j.actamat.2013.01.051.

[8] I. Gutierrez-Urrutia, D. Raabe, Dislocation and twin substructure evolution during strain hardening of an Fe-22 wt.% Mn-0.6 wt.% C TWIP steel observed by electron channeling contrast imaging, Acta Mater. 59 (2011) 6449–6462. doi:10.1016/j.actamat.2011.07.009.

[9] A. a. Saleh, C. Haase, E. V. Pereloma, D. a. Molodov, A. a. Gazder, On the evolution and modelling of brass-type texture in cold-rolled twinning-induced plasticity steel, Acta Mater. 70 (2014) 259–271. doi:10.1016/j.actamat.2014.02.033.

[10] D. Canadinc, H. Sehitoglu, H.J. Maier, D. Niklasch, Y.I. Chumlyakov, Orientation evolution in Hadfield steel single crystals under combined slip and twinning, Int. J. Solids Struct. 44 (2007) 34–50. doi:10.1016/j.ijsolstr.2006.04.011.

[11] D.R. Steinmetz, T. Jäpel, B. Wietbrock, P. Eisenlohr, I. Gutierrez-Urrutia, A. Saeed-Akbari, et al., Revealing the strain-hardening behavior of twinning-induced plasticity steels: Theory, simulations, experiments, Acta Mater. 61 (2013) 494–510. doi:10.1016/j.actamat.2012.09.064.

[12] B. Hutchinson, N. Ridley, On dislocation accumulation and work hardening in Hadfield steel, Scr. Mater. 55 (2006) 299–302. doi:10.1016/j.scriptamat.2006.05.002.

[13] J.K. Kim, L. Chen, H.S. Kim, S.K. Kim, Y. Estrin, B.C. De Cooman, On the tensile behavior of high-manganese twinning-induced plasticity steel, Metall. Mater. Trans. A Phys. Metall. Mater. Sci. 40 (2009) 3147–3158. doi:10.1007/s11661-009-9992-0.

[14] J. Kim, Y. Estrin, H. Beladi, I. Timokhina, K.G. Chin, S.K. Kim, et al., Constitutive modeling of the tensile behavior of Al-TWIP steel, Metall. Mater. Trans. A Phys. Metall. Mater. Sci. 43 (2012) 479–490. doi:10.1007/s11661-011-0898-2.

[15] W.S. Owen, M. Grujicic, Strain aging of austenitic Hadfield manganese steel, Acta Mater. 47 (1998) 111–126. doi:10.1016/S1359-6454(98)00347-4.

[16] D. Canadinc, C. Efstathiou, H. Sehitoglu, On the negative strain rate sensitivity of Hadfield steel, Scr. Mater. 59 (2008) 1103–1106. doi:10.1016/j.scriptamat.2008.07.027.

[17] H. Idrissi, K. Renard, D. Schryvers, P.J. Jacques, On the relationship between the twin internal structure and the work-hardening rate of TWIP steels, Scr. Mater. 63 (2010) 961–964. doi:10.1016/j.scriptamat.2010.07.016.

[18] Y.N. Dastur, W.C. Leslie, No Title, Metall. Mater. Trans. A. 12 (1981) 749.

[19] L. Remy, A. Pineau, Twinning and Strain-induced F.C.C. H.C.P. Transformation in the Fe-Mn-Cr-C System, (1976) 99–107.

[20] J.A. Venables, The nucleation and propagation of deformation twins, Solid State Commun. 2 (1964) 59.

[21] J.A. Venables, The electron microscopy of deformation twinning, J. Phys. Chem. Solids. 25 (1964) 685–692. doi:10.1016/0022-3697(64)90177-5.

[22] J. Friedel, Dislocations, Pergamon Press, Oxford, 1965.

[23] M.X. Huang, Z.Y. Liang, Z.C. Luo, Critical Assessment 15: Science of deformation and failure mechanisms in twinning induced plasticity steels, Mater. Sci. Technol. 31 (2015) 1265–1270. doi:10.1179/1743284715Y.0000000095.

[24] S. Allain, J.P. Chateau, D. Dahmoun, O. Bouaziz, Modeling of mechanical twinning in a high manganese content austenitic steel, Mater. Sci. Eng. A. 387-389 (2004) 272–276. doi:10.1016/j.msea.2004.05.038.

[25] J. Gil Sevillano, An alternative model for the strain hardening of FCC alloys that twin, validated for twinning-induced plasticity steel, Scr. Mater. 60 (2009) 336–339. doi:10.1016/j.scriptamat.2008.10.035.

[26] O. Bouaziz, N. Guelton, Modelling of TWIP effect on work-hardening, Mater. Sci. Eng. A. 319-321 (2001) 246–249. doi:10.1016/S0921-5093(00)02019-0.

[27] S.M. Toker, D. Canadinc, a. Taube, G. Gerstein, H.J. Maier, On the role of slip-twin interactions on the impact behavior of high-manganese austenitic steels, Mater. Sci. Eng. A. 593 (2014) 120–126. doi:10.1016/j.msea.2013.11.033.

[28] B. Bal, B. Gumus, G. Gerstein, D. Canadinc, H.J. Maier, On the micro-deformation mechanisms active in high-manganese austenitic steels under impact loading, Mater. Sci. Eng. A. 632 (2015) 29–34. doi:10.1016/j.msea.2015.02.054.

[29] B. Gumus, B. Bal, G. Gerstein, D. Canadinc, H.J. Maier, Twinning activity in high-manganese austenitic steels under high velocity loading, Mater. Sci. Technol. In press (2015). doi:10.1179/1743284715Y.0000000111.

[30] B.C. De Cooman, J. Kim, S. Lee, Heterogeneous deformation in twinning-induced plasticity steel, Scr. Mater. 66 (2012) 986–991. doi:10.1016/j.scriptamat.2012.02.028.

[31] K. Yan, D.G. Carr, M.D. Callaghan, K.D. Liss, H. Li, Deformation mechanisms of twinning-induced plasticity steels: In situ synchrotron characterization and modeling, Scr. Mater. 62 (2010) 246–249. doi:10.1016/j.scriptamat.2009.11.008.

[32] H. Idrissi, K. Renard, L. Ryelandt, D. Schryvers, P.J. Jacques, On the mechanism of twin formation in Fe-Mn-C TWIP steels, Acta Mater. 58 (2010) 2464–2476. doi:10.1016/j.actamat.2009.12.032.

[33] S. Dancette, L. Delannay, K. Renard, M. a. Melchior, P.J. Jacques, Crystal plasticity modeling of texture development and hardening in TWIP steels, Acta Mater. 60 (2012) 2135–2145. doi:10.1016/j.actamat.2012.01.015.

[34] M.N. Shiekhelsouk, V. Favier, K. Inal, M. Cherkaoui, Modelling the behaviour of polycrystalline austenitic steel with twinning-induced plasticity effect, Int. J. Plast. 25 (2009) 105–133. doi:10.1016/j.ijplas.2007.11.004.

[35] R. Quey, P.R. Dawson, F. Barbe, Large-scale 3D random polycrystals for the finite element method: Generation, meshing and remeshing, Comput. Methods Appl. Mech. Eng. 200 (2011) 1729–1745. doi:10.1016/j.cma.2011.01.002.

[36] F. Roters, P. Eisenlohr, L. Hantcherli, D.D. Tjahjanto, T.R. Bieler, D. Raabe, Overview of constitutive laws, kinematics, homogenization and multiscale methods in crystal plasticity finite-element modeling: Theory, experiments, applications, Acta Mater. 58 (2010) 1152–1211. doi:10.1016/j.actamat.2009.10.058.

[37] F. Barbe, L. Decker, D. Jeulin, G. Cailletaud, Intergranular and intragranular behavior of polycrystalline aggregates. Part 1: F.E. model, Int. J. Plast. 17 (2001) 513–536. doi:10.1016/S0749-6419(00)00061-9.

[38] P. Van Houtte, S. Li, M. Seefeldt, L. Delannay, Deformation texture prediction: From the Taylor model to the advanced Lamel model, 2005. doi:10.1016/j.ijplas.2004.04.011.

[39] R. a. Lebensohn, C.N. Tomé, A self-consistent anisotropic approach for the simulation of plastic deformation and texture development of polycrystals: Application to zirconium alloys, Acta Metall. Mater. 41 (1993) 2611–2624. doi:10.1016/0956-7151(93)90130-K.

[40] R. a. Lebensohn, C.N. Tomé, A self-consistent viscoplastic model: prediction of rolling textures of anisotropic polycrystals, Mater. Sci. Eng. A. 175 (1994) 71–82. doi:10.1016/0921-5093(94)91047-2.

[41] C.N. Tomé, R. a. Lebensohn, U.F. Kocks, A model for texture development dominated by deformation twinning: Application to zirconium alloys, Acta Metall. Mater. 39 (1991) 2667–2680. doi:10.1016/0956-7151(91)90083-D.

[42] S.R. Kalidindi, Modeling anisotropic strain hardening and deformation textures in low stacking fault energy fcc metals, Int. J. Plast. 17 (2001) 837–860. doi:10.1016/S0749-6419(00)00071-1.

[43] S.R. Kalidindi, Incorporation of deformation twinning in crystal plasticity models, J. Mech. Phys. Solids. 46 (1998) 267–290. doi:10.1016/S0022-5096(97)00051-3.

[44] I. Karaman, H. Sehitoglu, K. Gall, Y.I. Chumlyakov, H.J. Maier, Deformation of single crystal hadfield steel by twinning and slip, Acta Mater. 48 (2000) 1345–1359. doi:10.1016/S1359-6454(99)00383-3.

[45] I. Karaman, H. Sehitoglu, K. Gall, Y.I. Chumlyakov, On The Deformation Mechanisms in Single Crystal Hadfield Manganese Steels, Scr. Mater. 38 (1998) 1009–1015. doi:10.1016/S1359-6462(97)00581-2.

[46] I. Karaman, H. Sehitoglu, Y.I. Chumlyakov, H.J. Maier, I. V. Kireeva, Extrinsic stacking faults and twinning in Hadfield manganese steel single crystals, Scr. Mater. 44 (2001) 337–343. doi:10.1016/S1359-6462(00)00600-X.

[47] I. Karaman, H. Sehitoglu, a. . Beaudoin, Y.. Chumlyakov, H.. Maier, C.. Tomé, Modeling the deformation behavior of Hadfield steel single and polycrystals due to twinning and slip, Acta Mater. 48 (2000) 2031–2047. doi:10.1016/S1359-6454(00)00051-3.

[48] D. Canadinc, H. Sehitoglu, H.J. Maier, The role of dense dislocation walls on the deformation response of aluminum alloyed hadfield steel polycrystals, Mater. Sci. Eng. A. 454-455 (2007) 662–666. doi:10.1016/j.msea.2006.11.122.

[49] D. Canadinc, E. Biyikli, T. Niendorf, H.J. Maier, Experimental and numerical investigation of the role of grain boundary misorientation angle on the dislocation-grain boundary interactions, Adv. Eng. Mater. 13 (2011) 281–287. doi:10.1002/adem.201000229.

[50] E. Biyikli, D. Canadinc, H.J. Maier, T. Niendorf, S. Top, Three-dimensional modeling of the grain boundary misorientation angle distribution based on two-dimensional experimental texture measurements, Mater. Sci. Eng. A. 527 (2010) 5604–5612. doi:10.1016/j.msea.2010.05.037.

[51] C.N. Tomé, R.A. Lebensohn, Manual for Code Visco-Plastic Self-Consistent (VPSC) version 5, 2000.

[52] U.F. Kocks, C.N. Tome, H.R. Wenk, Texture and Anisotropy, 2nd ed., Cambridge University Press, 2000.

[53] C. Tome, G.R. Canova, U.F. Kocks, N. Christodoulou, J.J. Jonas, The relation between macroscopic and microscopic strain hardening in F.C.C. polycrystals, Acta Metall. 32 (1984) 1637–1653. http://www.sciencedirect.com/science/article/pii/0001616084902220.

[54] C.N. Tome, R.A. Lebensohn, Manual for Code Visco-Plastic Self-Consistent (VPSC) version 7d, 2012.

[55] D. Canadinc, H. Sehitoglu, H.J. Maier, Y.I. Chumlyakov, Strain hardening behavior of aluminum alloyed Hadfield steel single crystals, Acta Mater. 53 (2005) 1831–1842. doi:10.1016/j.actamat.2004.12.033.

[56] K.M. Rahman, N.G. Jones, D. Dye, Micromechanics of twinning in a TWIP steel, Mater. Sci. Eng. A. 635 (2015) 133–142. doi:10.1016/j.msea.2015.03.082.

[57] K.M. Rahman, V. a. Vorontsov, D. Dye, The effect of grain size on the twin initiation stress in a TWIP steel, Acta Mater. 89 (2015) 247–257. doi:10.1016/j.actamat.2015.02.008.

[58] E. Schmid, W. Boas, Kristallplastizität: Mit Besonderer Berücksichtigung der Metalle, Springer-Verlag Berlin and Heidelberg GmbH Co., KG, Germany, 1935.

[59] D. Canadinc, H. Sehitoglu, H.J. Maier, P. Kurath, On the incorporation of length scales associated with pearlitic and bainitic microstructures into a visco-plastic self-consistent model, Mater. Sci. Eng. A. 485 (2008) 258–271. doi:10.1016/j.msea.2007.08.049.

[60] S. Kibey, J.B. Liu, D.D. Johnson, H. Sehitoglu, Predicting twinning stress in fcc metals: Linking twin-energy pathways to twin nucleation, Acta Mater. 55 (2007) 6843–6851. doi:10.1016/j.actamat.2007.08.042.

[61] S. Mahajan, G.Y. Chin, Formation of deformation twins in f.c.c. crystals, Acta Metall. 21 (1973) 1353–1363.

[62] T.S. Byun, On the stress dependence of partial dislocation separation and deformation microstructure in austenitic stainless steels, Acta Mater. 51 (2003) 3063–3071. doi:10.1016/S1359-6454(03)00117-4.

[63] J.B. Cohen, J. Weertman, A dislocation model for twinning in f.c.c. metals, Acta Metall. 11 (1963) 996–998.

[64] R. Ueji, N. Tsuchida, D. Terada, N. Tsuji, Y. Tanaka, a. Takemura, et al., Tensile properties and twinning behavior of high manganese austenitic steel with fine-grained structure, Scr. Mater. 59 (2008) 963–966. doi:10.1016/j.scriptamat.2008.06.050.

[65] J.W. Christian, S. Mahajan, Deformation twinning, Prog. Mater. Sci. 39 (1995) 1–157. doi:10.1016/0079-6425(94)00007-7.

[66] M.J.J. W., Stronger, Tougher Steels, Sci. 320. (2008) 1022–1023.

[67] K. Kormi, D.C. Webb, W. Johnson, The application of the FEM to determine the response of a pretorsioned pipe cluster to static or dynamic axial impact loading, Comput. Struct. 62 (1997) 353–368.

[68] S.L. Raykhere, P. Kumar, R.K. Singh, V. Parameswaran, Dynamic shear strength of adhesive joints made of metallic and composite adherents, Mater. Des. 31 (2010) 2102–2109. doi:10.1016/j.matdes.2009.10.043.

2 CHAPTER 2

MULTI-SCALE MODELING OF THE IMPACT RESPONSE OF A STRAIN RATE SENSITIVE HIGH-MANGANESE AUSTENITIC STEEL

2.1 Introduction

Austenitic high-manganese (Mn) steels, a class of high strength steels, have received considerable attention since they offer a rare combination of exceptional work hardening capacity, high wear and abrasion resistance, high strength and significant ductility [1-3]. These extraordinary mechanical properties have been subject to several studies [3-9], many of which revealed that the main mechanism underlying the observed mechanical behavior is the presence of twins in the microstructure accompanied by additional microstructural features, such as stacking faults, dynamic strain aging (DSA) and interaction of twins with dislocations [6-9]. Simultaneous activity of all of the aforementioned micro-deformation mechanisms result in the improved strength and work hardening capacity of this class of steels, where all these mechanisms constitute obstacles against gliding dislocations [6-9]. However, the complexity of the deformation behavior of these materials makes it difficult to clearly distinguish between the relative contributions of the hardening mechanisms.

A very good example to this complicated microstructure is that of Hadfield steel, a high-Mn austenitic steel with a face-centered cubic (fcc) structure at room temperature. Hadfield steel is well known for its deformation by both slip and twinning [6, 10], where the two mechanisms interact and further promote work hardening concomitant with increasing strain. To add further to the complexity of micro-deformation mechanisms, glide dislocations tend to form high-density dislocation walls (HDDWs), which effectively hinder active glide dislocations from moving further, contributing to the unusual strain hardening exhibited by this material [11, 12]. However, dislocations are prevented from gliding not by twin

boundaries or HDDWs only, but also by carbon (C), which can diffuse within the matrix throughout the deformation, as it becomes easily excited by the energy provided by the applied stresses [13].

The excited C atoms diffuse within the matrix, however; when they meet dislocations at interstitial zones, they prevent dislocations from gliding further, which is referred to as pinning of the dislocation by the C atom [1, 13]. This, indeed, gives way to DSA [1, 13], which further adds to the complexity of the microstructure by promoting strain rate sensitivity (SRS) and negative strain rate sensitivity (NSRS) [13]. Specifically, as a steel is deformed at a faster rate, the rate of generation of forest dislocations increases, as well, leading to an increased level of stress at the same strain value, which is known as the SRS [13]. In Hadfield steel, however; the diffusion velocity of C also increases concomitant with strain rate. At lower strain rates, the C atoms stay longer at an interstitial site, potentially pinning a dislocation for a longer period, which is a positive contribution in terms of strain hardening. However, as the deformation rate increases, C atoms start to diffuse much faster, and they cannot pin dislocations for extended periods, which indeed takes away an important contribution to the overall hardening: the result is softening, and even though the strain rate increases, the material attains lower levels of stress at the same strains, which is known as the NSRS [13]. The NSRS, however; is eliminated at very high strain rates, such that the missing contribution to the overall hardening due to the pinning of dislocations becomes negligible as compared to the significant forest hardening, which constitutes the major mechanism of hardening at elevated rates of deformation [13].

Despite their complicated micro-deformation mechanisms, other high-Mn austenitic steels with similar microstructures, such as the twinning-induced plasticity (TWIP) steels, continue to attract attention and find use in applications, mainly owing to their superior mechanical properties [9, 14-16]. Automotive industry and other load bearing applications

utilize high-Mn steels at an increasing rate, and ballistic applications constitute another potential area that may utilize this class of steels. For all these applications, however; resistance to impact loading and understanding the deformation response under impact becomes of utmost importance [10]. Considering the design process of any commercial product, on the other hand, one realizes that the capability to realistically predict the impact response of these alloys by numerical modeling is warranted, which constitutes the motivation of the current work.

The impact performance of a material is governed by its microstructure, and the corresponding parameters, such as grain boundaries, grain size, precipitates and delaminations, and the material's ductile-to-brittle transition temperature (DBTT) altogether dictate the response to impact loading [17-20]. Another important parameter affecting the impact response is the texture of the material, which defines the grain boundary – dislocation interactions, and thus, the crack propagation behavior under impact loading, as well as the degree of anisotropy, which dictates the relative slip activity in each grain [17], warranting incorporation of anisotropy effects into the design process.

The current study was undertaken with the motivation of addressing this issue, such that a combined experimental and numerical approach is proposed to predict the impact response of high-Mn austenitic steels in a realistic manner. For this purpose, uniaxial tensile deformation and impact responses of Hadfield steel were experimentally monitored, where the uniaxial deformation experiments featured four different strain rates ranging from moderate to high in order to also assess the role of NSRS exhibited by this material. Finite element (FE) simulations of the impact experiments were carried out, where the roles of texture, geometry and strain rate sensitivity were successfully taken into account all at once by incorporating the proper multi-axial material flow rule obtained from crystal plasticity simulations into the FE analysis. Specifically, crystal plasticity was utilized to obtain the

multi-axial flow rule at different strain rates based on the experimental deformation response under uniaxial tensile loading, and the equivalent stress – equivalent strain response was then incorporated into the FE model for the sake of a more representative hardening rule under impact loading. The current results demonstrate that reliable predictions can be obtained by proper coupling of crystal plasticity and FE analysis even if the experimental flow rule of the material is acquired under uniaxial loading and at moderate strain rates that are significantly slower than those attained during impact loading. Overall, the approach presented herein constitutes an important guideline for the design process of impact bearing applications utilizing high-Mn austenitic steels.

2.2 Materials and Methods

The material investigated in this study is Hadfield steel, an high-Mn austenitic steel with a fcc structure, and has a chemical composition of 12.44 wt% Mn, 1.10 wt% C and balance iron. Small-scale dog-bone shaped tension samples were extracted from railroad frogs taken from service with the aid of electro-discharge machining to avoid any process-induced residual stresses and strains on the samples. The room temperature (RT) monotonic tensile deformation experiments were carried out on a servo-hydraulic test frame equipped with a digital controller and a miniature extensometer of 3 mm gauge length. The results revealed a significant SRS prevalent in Hadfield steel polycrystals within the strain rate range of 1×10^{-4} 1/s to 1×10^{-1} 1/s (Figure 2.2.1). A serrated flow was exhibited by the material at all strain rates, however; the associated instability was much more prominent at 1×10^{-3} 1/s, where NSRS was prevalent as evidenced by the lower stress levels attained despite the ten-fold increase in the strain rate from 1×10^{-4} 1/s to 1×10^{-3} 1/s.

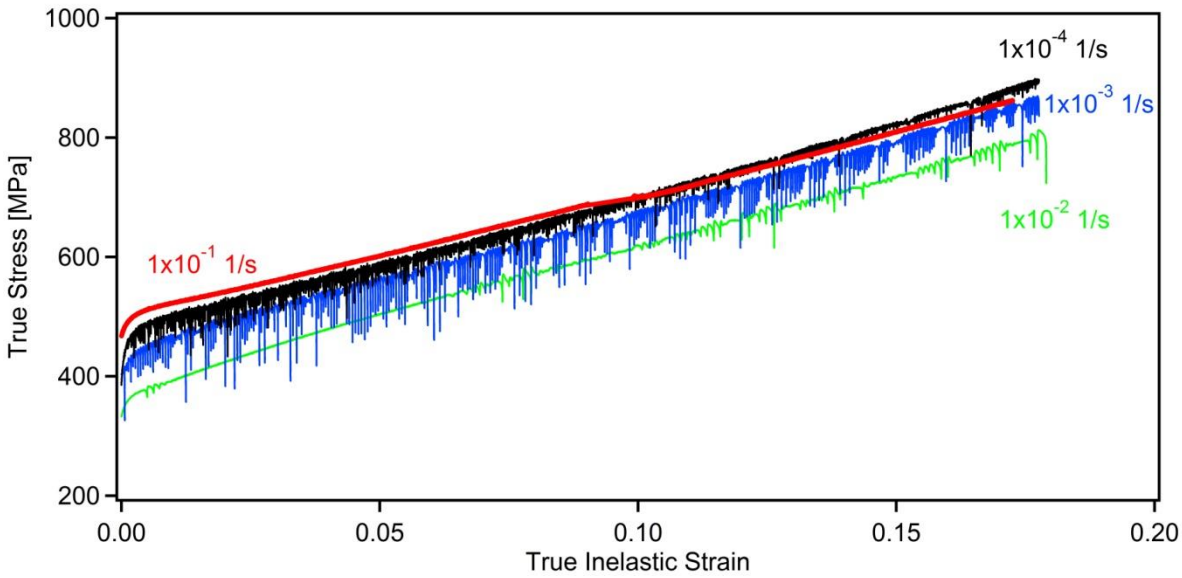

Figure 2.2.1. RT uniaxial tensile deformation response of Hadfield steel obtained at different strain rates, demonstrating the NSRS. Data was recompiled from [13].

The impact samples were extracted from both the same Hadfield railroad frog with dimensions of 2.8 mm × 25 mm × 4 mm, featuring a 60˚ notch with a radius of 0.1 mm and a depth of 1 mm [17]. The specimens were mechanically polished down to a 4000 grit size in order to minimize the detrimental effects of machined surfaces on the impact response. The impact experiments were conducted at RT, and the specimens were subjected to deformation with an impact energy of 50 J and at a velocity of 3.8 m/s, where 8000 data points were collected during each experiment with a data acquisition frequency of 2 MHz. For both uniaxial deformation and impact experiments, three companion samples were tested in each case in order to ensure repeatability. The initial textures of the samples prior to deformation were determined by X-ray diffraction.

2.3 Results and Discussion

2.3.1 Finite Element Simulations of Experimental Impact Response of Hadfield Steel

It is well known that very large deformations taking place within very short time periods constitute the major difficulty of FE simulations of impact loading [17, 21, 22]. Specifically, the available time period is insufficient for the stabilization of the computed displacements in the case of impact loading, such that the material's behavior significantly deviates under this dynamic type of loading from that under normal conditions owing to the nonlinear behavior under dynamic loading [17]. The current FE simulations of the impact behavior were carried out utilizing the ANSYS® 15 commercial software and the FE analysis was based on an explicit dynamics system, where the LS-DYNA® solver was employed in computations for the sake of a reliable nonlinear dynamic analysis.

The Lagrangian formulation and multilinear isotropic hardening were chosen to represent the nonlinearity and the plastic flow, respectively. A fine "MultiZone" mesh was constructed with 13530 nodes and 11060 quadrilateral elements, where the geometry was automatically decomposed into a hex mesh, increasing both the accuracy and computational efficiency of the simulations. The notch region was meshed with an element size of 0.1 mm, and the mesh had an orthogonal quality of 0.98 (out of 1.0). All contact regions of the impact sample were assumed to be frictional, and the corresponding static and dynamic friction coefficients were set to 0.2 and 0.09, respectively [17]. As for the boundary conditions, a nodal displacement was imposed on the top notch surface and fixed supports were placed at the right/left sides and on the bottom surface. Beyond the fracture point of the specimens, i.e. where the sample – hammer contact terminates, the equivalent plastic strain (EPS) criterion was utilized to define failure of the material, namely an EPS of 0.68 was preset as the failure

initiation point. The Cartesian coordinate system was considered while designating the dimensions and constraints.

The first set of simulations made use of the experimental RT uniaxial tensile deformation response of Hadfield steel obtained at a strain rate of 1×10^{-4} 1/s to define the multilinear isotropic hardening rule (Figure 2.3.1.1). This strain rate is rather a moderate strain rate typically utilized in laboratory experiments employed to characterize the material's deformation response [17]. It is evident that the corresponding simulation result significantly differs from the experimentally measured impact behavior, indicating that the flow rule of the material should be based on experiments featuring much higher strain rates as the impact deformation itself takes place very rapidly. Thus, in order to assess the role of strain rate, FE simulations considering higher rates of deformation, namely 1×10^{-1} 1/s, 1×10^{-2} 1/s and 1×10^{-3} 1/s, were carried out (Figure 2.3.1.2). As expected, a comparison of experimental and simulated impact responses (based on four different strain rates) expressed in terms of force-time data (Figures 2.3.1.1 and 2.3.1.2) indicates the best predictions are made when the flow rule is based on the experimental deformation response obtained at the strain rate of 1×10^{-3} 1/s. A further look at the results presented in Figures 2.3.1.1 and 2.3.1.2 reveal a more interesting fact: the second best prediction is obtained when the flow rule is defined based on the uniaxial tensile deformation response obtained at a strain rate of 1×10^{-4} 1/s. This implies that the experimental data obtained within the NSRS range should not be utilized to define the hardening rule when constructing a FE model to predict impact response, regardless of the strain rate.

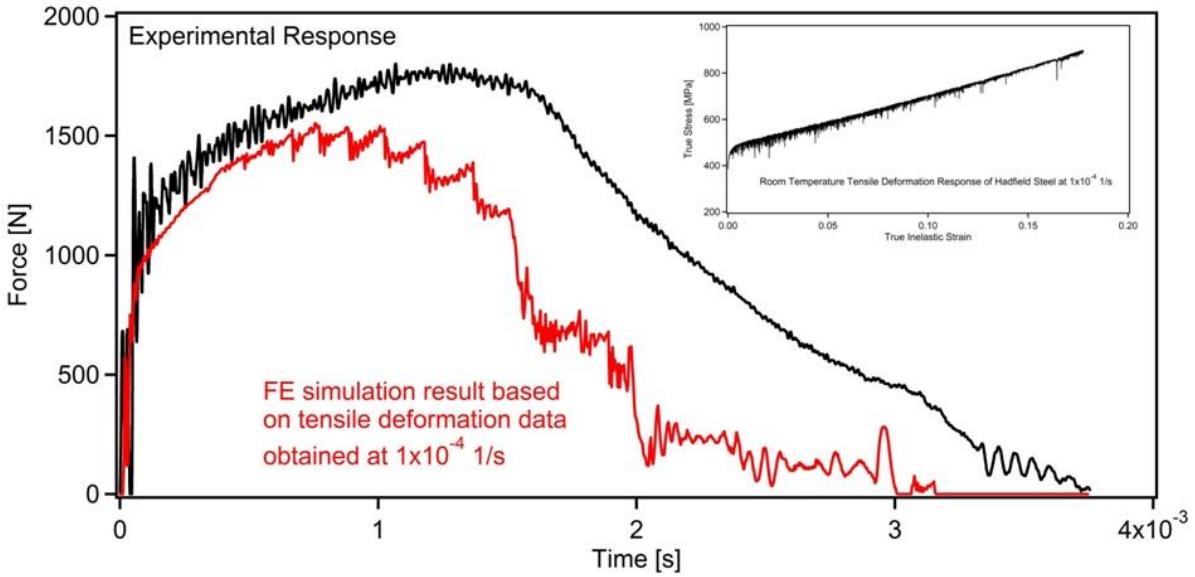

Figure 2.3.1.1. The RT experimental impact response of Hadfield steel and the corresponding FE simulation result, where the flow rule was defined based on the experimental uniaxial tensile deformation response obtained at a strain rate of 1×10^{-4} 1/s.

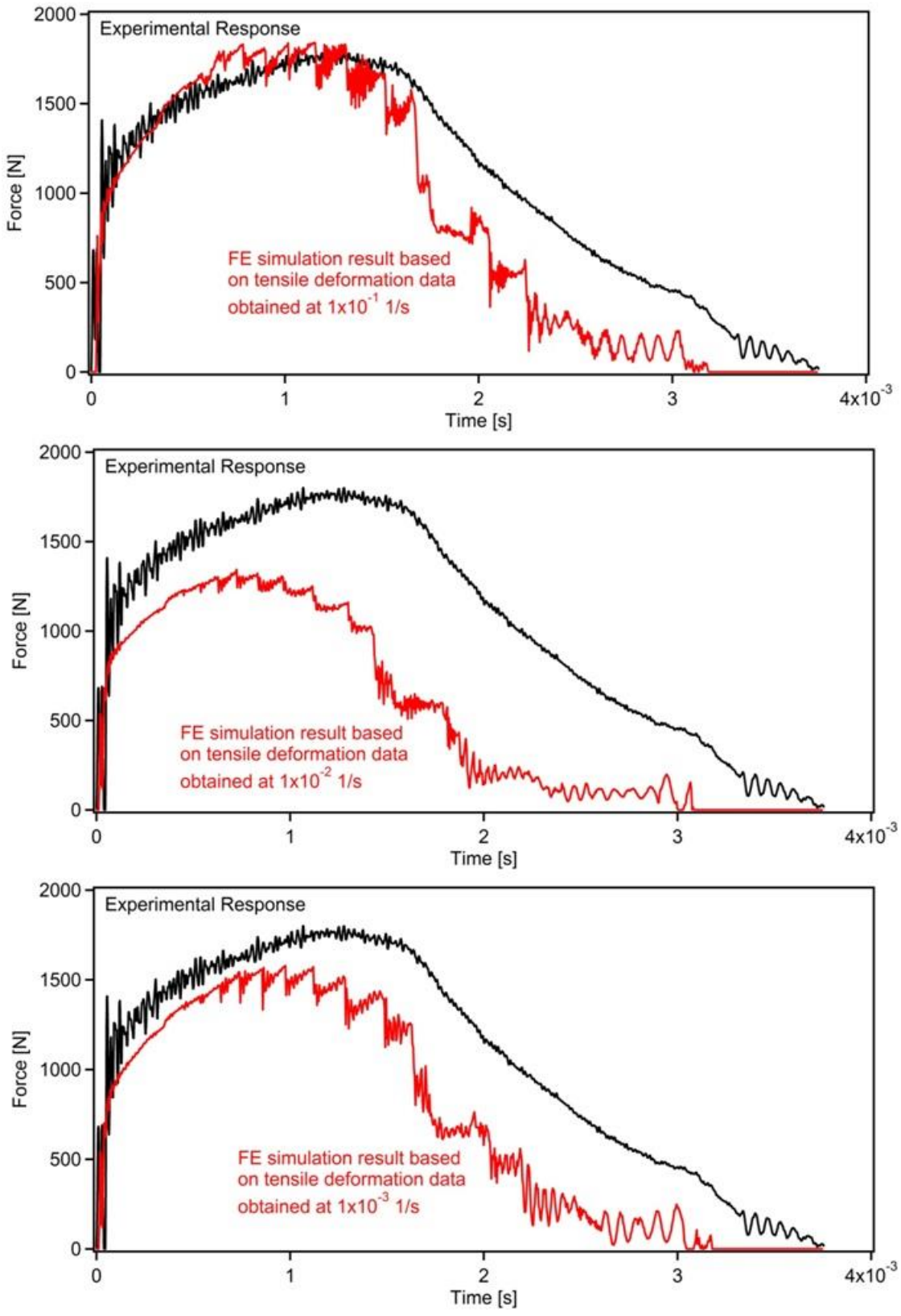

Figure 2.3.1.2. A comparison of the RT experimental impact response of Hadfield steel and the corresponding FE simulation results, where the flow rule was defined based on the experimental uniaxial tensile deformation responses obtained at strain rates of 1×10^{-1} 1/s, 1×10^{-2} 1/s and 1×10^{-3} 1/s.

Overall, all of the FE simulation results presented in Figures 2.3.1.1 and 2.3.1.2 exhibited noticeable deviation from the experimental impact response, implying that the provided hardening response based on the experimental uniaxial tensile deformation data was not sufficiently representative of the material's mechanical behavior under impact loading at any of the considered strain rates. Further simulations featuring a finer mesh were also carried out in order to question the numerical procedure, however; the same deviation from the experimental results persisted.

It has recently been demonstrated that a multiaxial stress-strain state is present in the critical region of the sample [17], and a comparison of normal and von Mises stress distributions reveals that employment of the uniaxial tensile deformation data as the input defining the material's flow rule under impact loading is not appropriate (Figure 2.3.1.3). Even though this approach might be appropriate for an isotropic material, it falls far from being realistic for a textured material exhibiting a significant degree of anisotropy [17]. The numerical analyses carried out until this point (Figures 2.3.1.1-2.3.1.3) clearly demonstrate the need for a proper representation of microstructure under impact loading, in addition to the strain rate effects.

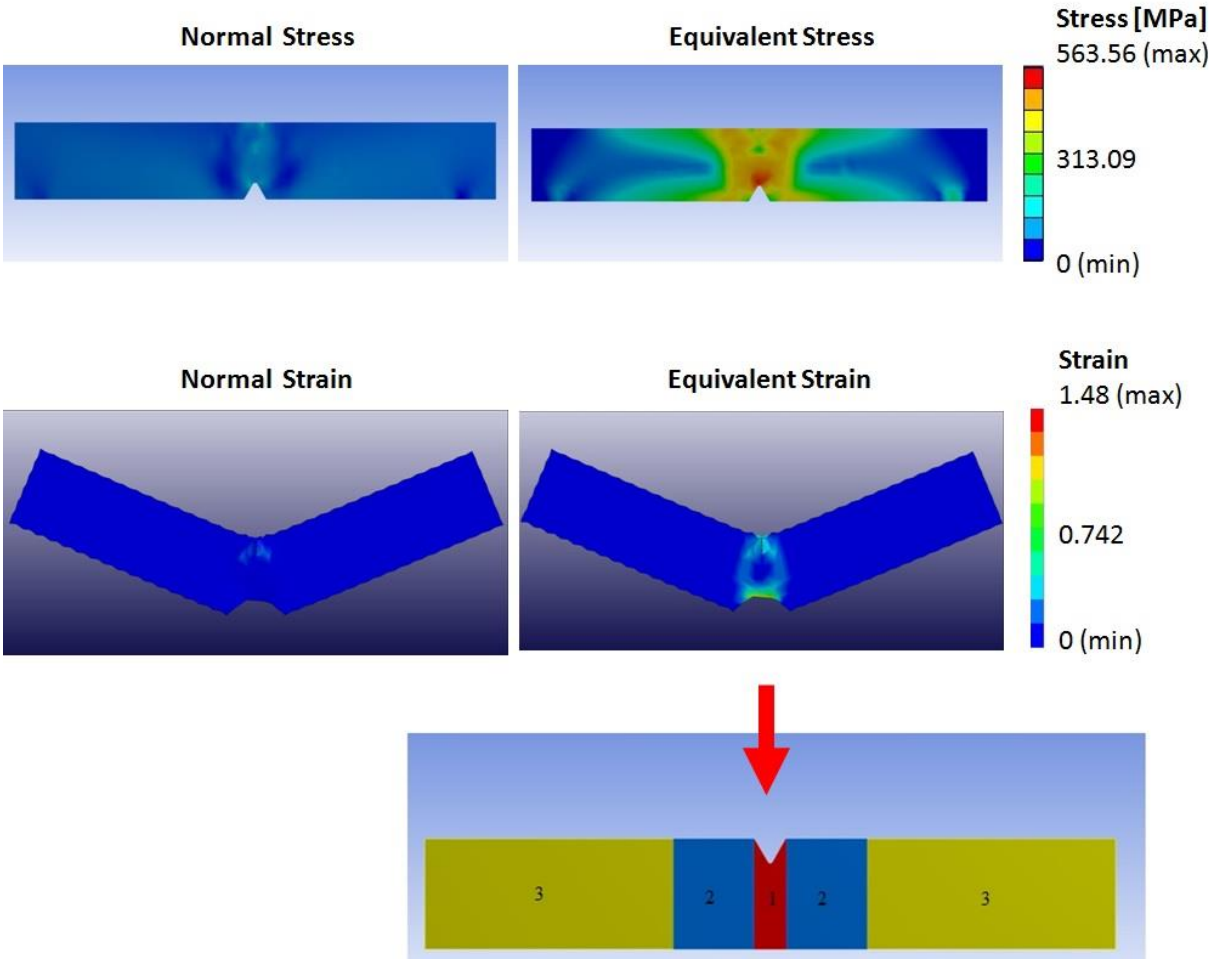

Figure 2.3.1.3. A material-independent FE simulation of impact loading demonstrating the typical distribution of normal and equivalent stress-strain fields (above the arrow), and the corresponding division of sample geometry based on stress intensities within the sample [17].

2.3.2 Incorporation of the Role of Microstructure into the Finite Element Simulations through Crystal Plasticity

In order to utilize a proper flow rule to define hardening of Hadfield steel during impact, and account for the role of texture and the corresponding anisotropy – in addition to the strain rate effects – in the current FE simulations, a crystal plasticity approach was adopted. Specifically, based on the aforementioned analysis of stress-strain distributions upon impact loading (Figure 2.3.1.3), a flow rule based on equivalent stress-strain response was defined. In

order to do so, a visco-plastic self-consistent (VPSC) algorithm was utilized to predict the von Mises stress-strain behavior of the material based on the experimental uniaxial tensile deformation data. Even though an alternative way of establishing the equivalent stress-strain response would have been carrying out multiaxial deformation experiments, the current methodology is much more efficient due to the impractical multiaxial experiments, especially in the case of high strain rates.

A successful crystal plasticity model should both predict the macroscopic deformation response and capture the deformation characteristics at the slip system level [23], such that the deformation response could be predicted under any type of loading [24]. With this motivation, the deformation of Hadfield steel was modeled at the microscopic level for each strain rate considered herein based on the corresponding experimentally obtained uniaxial deformation response (Figures 2.3.2.1-2.3.2.4). The VPSC model utilizes the initial texture of the material as an input, such that the loads on each grain, and thereby the slip activities in each grain, are dictated by the texture of the material [25-27]. Thereafter, the same micro level model established for each strain rate was utilized to predict the corresponding equivalent stress-strain response (Figure 2.3.2.1-2.3.2.4), which can be utilized as a proper flow rule for the impact simulations, as discussed before.

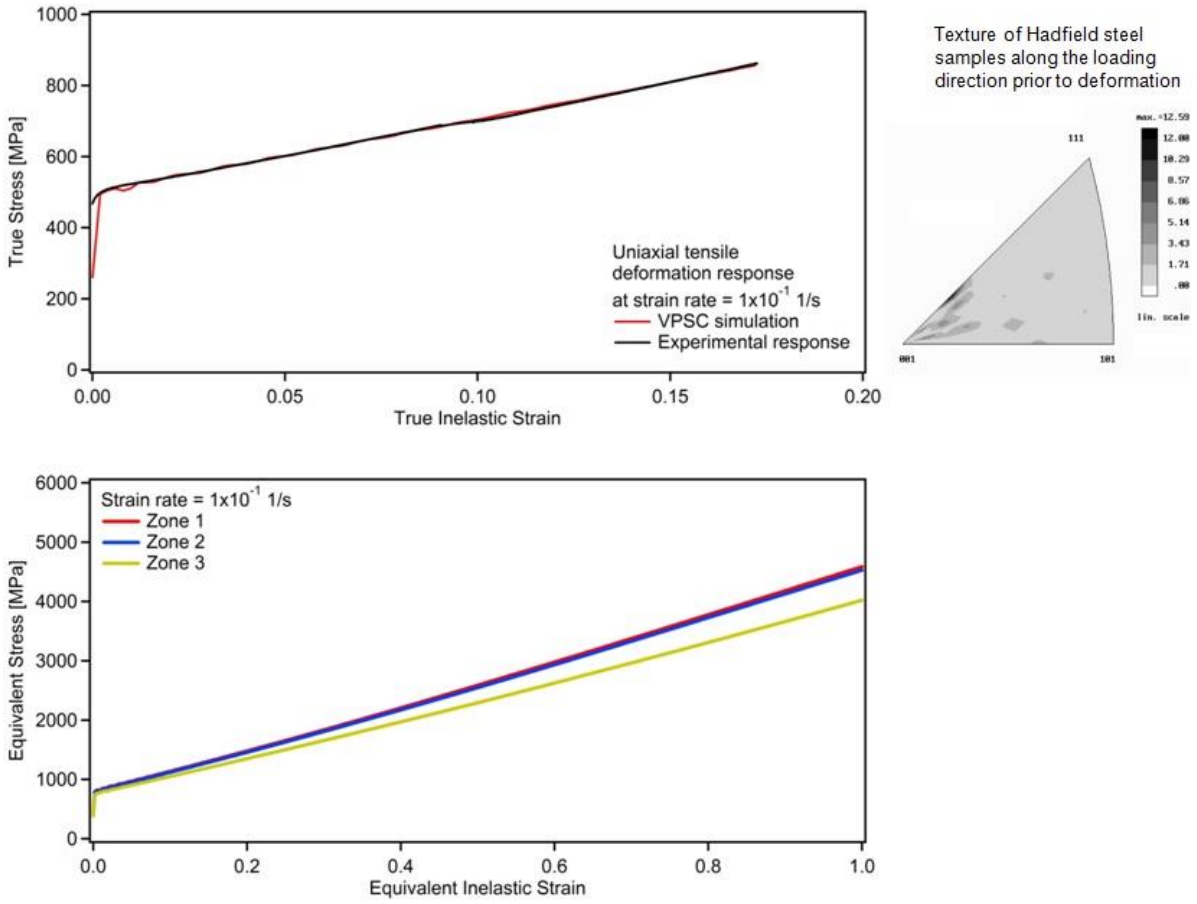

Figure 2.3.2.1. Top: VPSC simulation of the RT experimental uniaxial tensile deformation of Hadfield steel at a strain rate of 1×10^{-1} 1/s, and the corresponding initial texture along the loading direction (representative of the texture of all companion samples). Bottom: the corresponding predicted equivalent stress-strain response for each zone within the impact sample based on the distribution of stress concentration (Figure 2.3.1.3).

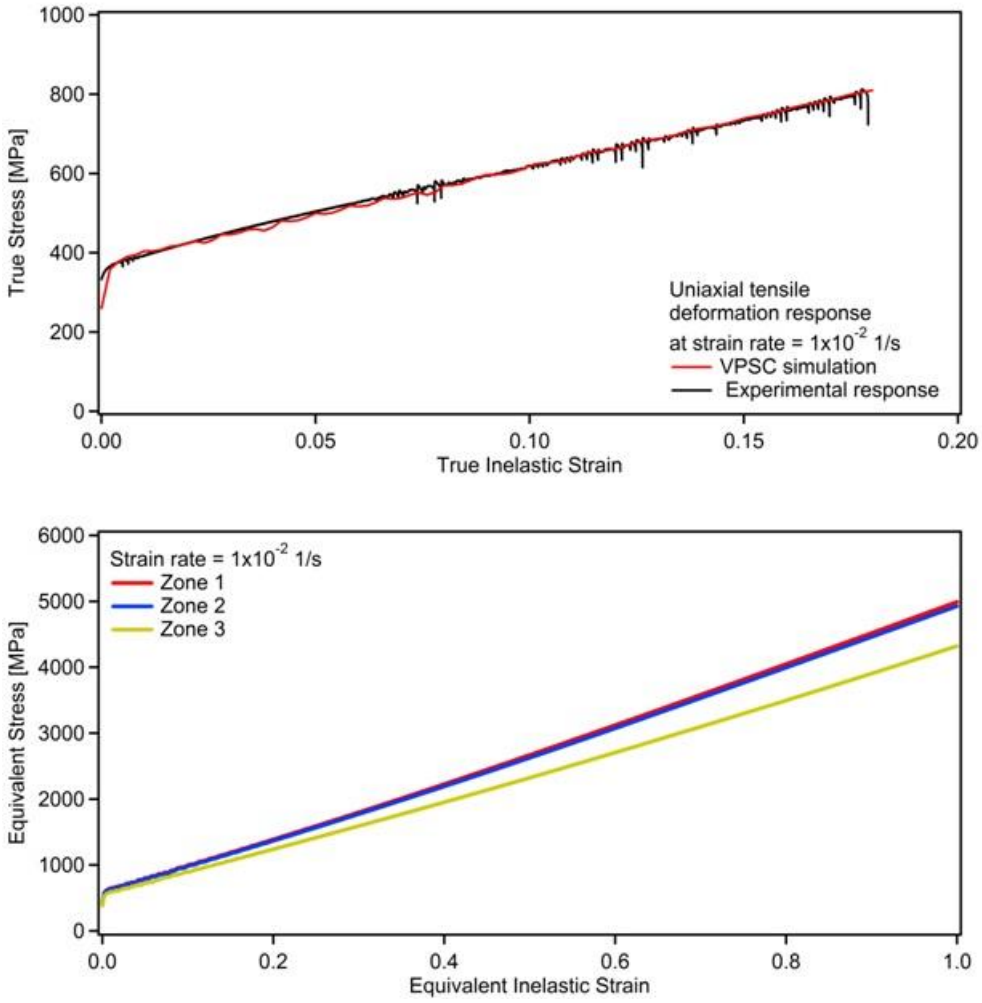

Figure 2.3.2.2. Top: VPSC simulation of the RT experimental uniaxial tensile deformation of Hadfield steel at a strain rate of 1×10^{-2} 1/s. Bottom: the corresponding predicted equivalent stress-strain response for each zone within the impact sample based on the distribution of stress concentration (Figure 2.3.1.3).

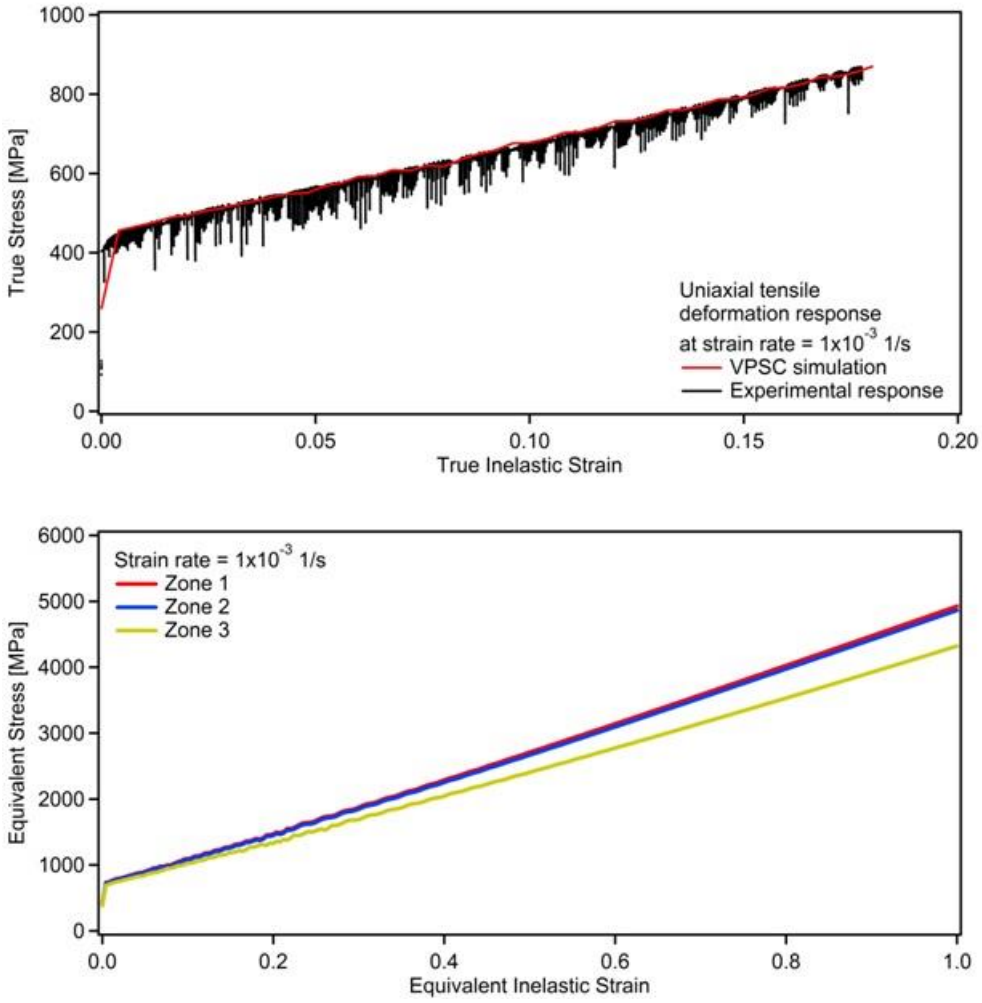

Figure 2.3.2.3. Top: VPSC simulation of the RT experimental uniaxial tensile deformation of Hadfield steel at a strain rate of 1×10^{-3} 1/s. Bottom: the corresponding predicted equivalent stress-strain response for each zone within the impact sample based on the distribution of stress concentration (Figure 2.3.1.3).

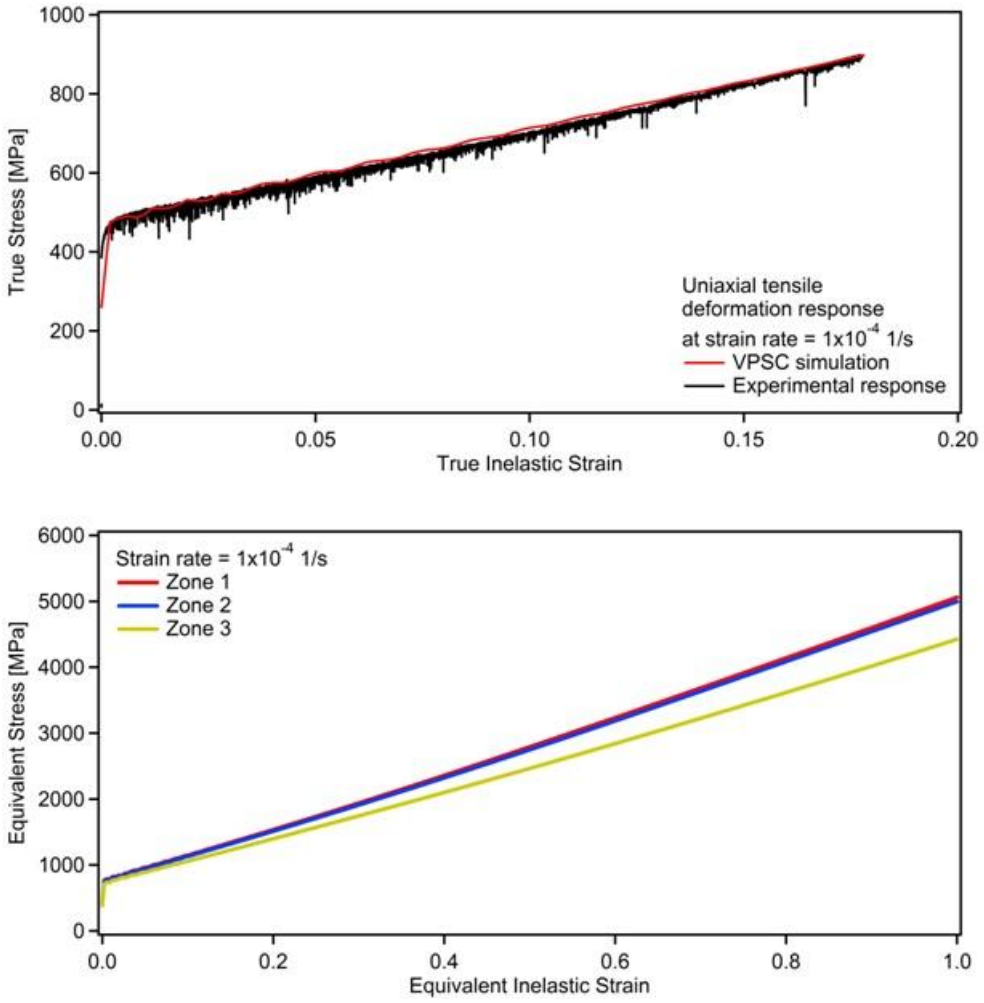

Figure 2.3.2.4. Top: VPSC simulation of the RT experimental uniaxial tensile deformation of Hadfield steel at a strain rate of 1×10^{-4} 1/s. Bottom: the corresponding predicted equivalent stress-strain response for each zone within the impact sample based on the distribution of stress concentration (Figure 2.3.1.3).

The VPSC algorithm employed in the current study considers plastic deformation only, which takes place when one or more slip or twinning systems become active. For a slip system s, the corresponding resolved shear stress (τ_{RSS}^{s}) facilitating plastic deformation can be described in vector form based on the Schmid (m_i^s) and the applied stress (σ_i) tensors:

$$\tau_{RSS}^{s} = m_i^s \sigma_i \tag{1}$$

The nonlinear shear strain rate in the system *s* can be described as a function of τ_{RSS}^{s}:

$$\dot{\gamma}^s = \dot{\gamma}_0 \left(\frac{\tau_{RSS}^{s}}{\tau_0^s} \right)^n = \dot{\gamma}_0 \left(\frac{m_i^s \sigma_i}{\tau_0^s} \right)^n \tag{2}$$

where $\dot{\gamma}_0$ is a reference rate, τ_0^s is the threshold stress corresponding to this reference rate, and *n* is the inverse of the rate sensitivity index. When the contributions of all active systems in a single grain are superposed and pseudolinearized [25]:

$$\dot{\varepsilon}_i = \left[\dot{\gamma}_0 \sum_{1}^{s} \frac{m_i^s m_j^s}{\tau_0^s} \left(\frac{m_k^s \sigma_k}{\tau_0^s} \right)^{n-1} \right] \sigma_j = M_{ij}^{c(\mathrm{sec})}(\tilde{\sigma}) \sigma_j \tag{3}$$

where $M_{ij}^{c(\mathrm{sec})}$ is the secant visco-plastic compliance of the crystal which gives the instantaneous relation between stress and strain rate. At the polycrystal level, this relationship assumes the following form [25]:

$$\dot{E}_i = M_{ij}^{(\mathrm{sec})}(\tilde{\Sigma}) \Sigma_j + \dot{\Sigma}^0 \tag{4}$$

where $\dot{E}_i$ and Σ represent the polycrystal strain rate and applied stress, respectively.

In a continuum comprising a matrix and inclusions, the deviations in strain rate and stress of the inclusions from those of the matrix can be defined as:

$$\tilde{\dot{\varepsilon}}_k = \dot{\varepsilon}_k - \dot{E}_k \tag{5}$$

$$\tilde{\sigma}_j = \sigma_j - \Sigma_j \tag{6}$$

where $\dot{\varepsilon}_k$ and σ_j stand for the local (grain level) strain rate and stress. When the Eshelby inclusion formulation is employed to solve the stress equilibrium, one can obtain [26]:

$$\tilde{\dot{\varepsilon}} = -\tilde{M} : \tilde{\sigma} \tag{7}$$

The interaction tensor $\tilde{M}$ is defined as

$$\tilde{M} = n'(I - S)^{-1} : S : M^{(\mathrm{sec})} \tag{8}$$

where $M^{(\mathrm{sec})}$ is the secant compliance tensor for the polycrystal aggregate and S is the visco-plastic Eshelby tensor [26]. In Equation 8, an effective value of n'=1 was used, which ensures a rigid interaction [25].

Substitution of equations 3 and 4 into Equation 7 yields the macroscopic secant compliance, $M^{(\mathrm{sec})}$, and the macroscopic strain rate is evaluated by taking the weighted average of crystal strain rates over all the grains as in Equation 9:

$$M^{(\mathrm{sec})} = \left\langle M^{c(\mathrm{sec})} : \left(M^{c(\mathrm{sec})} + \tilde{M}\right)^{-1} : \left(M^{(\mathrm{sec})} + \tilde{M}\right) \right\rangle \tag{9}$$

Iterative solution of the Equations 3, 7 and 9 gives the stress in each grain, the crystal's compliance tensor, and the polycrystal compliance consistent with the applied strain rate $\dot{E}_i$. In this work, the term *n* in Equation 2 was chosen as 20, which makes the formulation rate insensitive [25]. This sounds contradictory to the overall aim of incorporating the NSRS of Hadield steel into the simulations, however; it should be noted that the uniaxial deformation response at each strain rate was modeled separately rather than utilizing a single micro-deformation model accounting for the SRS. Therefore, the term *n* in Equation 2 was assigned a value to ensure rate insensitivity within the same simulation, or in other words, for each case. One reason for this is that, to the best of the authors' knowledge, a crystal plasticity model capable of predicting the NSRS exhibited by Hadfield steel has not been forwarded yet. Furthermore, the incorporation of NSRS requires coupling of crystal plasticity with atomistic

simulations to properly account for the diffusivity of C and the corresponding consequences, which is beyond the scope of the current work.

The rate of overall dislocation density can be expressed as:

$$\dot{\rho} = \sum_{n} \left\{ k_1 \sqrt{\rho} - k_2 \rho \right\} \left| \dot{\gamma}^n \right| \tag{10}$$

where k_1 and k_2 are geometric constants that define the athermal (statistical) storage of the moving dislocations [26]. The flow stress τ is defined in the traditional Taylor hardening format as:

$$\tau - \tau_0 = \alpha \mu b \sqrt{\rho} \tag{11}$$

where α is the dislocation interaction parameter and τ_0 is a reference strength, which is related to deformation at the grain level. The reference strength value for Hadfield steel was determined as 132 MPa in previous work [12], where the 0.2% offset yield strength value is normalized by the Taylor factor. The Taylor factor for the current materials was determined based on the experimentally measured texture [24], and it is about 3.11, which represents a slightly textured material as compared to the fully random texture case that has a Taylor factor of 3.06. From Equation 11, with τ_0 constant, the rate of the flow stress is obtained by taking the time derivative as,

$$\dot{\tau} = \frac{\alpha \mu b \dot{\rho}}{2\sqrt{\rho}} \tag{12}$$

Substituting Equation 10 into Equation 12 results in:

$$\dot{\tau} = \sum_{n} \left\{ k_1 \frac{\alpha \mu b}{2} - k_2 \frac{\alpha \mu b}{2} \sqrt{\rho} \right\} \left| \dot{\gamma}^n \right| \tag{13}$$

From Equation 11, the following identity is obtained for the square root of the density of dislocations:

$$\sqrt{\rho} = \frac{\tau - \tau_0}{\alpha \mu b} \tag{14}$$

Once Equation 14 is substituted into Equation 13, the rate of flow stress evolution is given by:

$$\dot{\tau} = \sum_n \left\{ k_1 \frac{\alpha \mu b}{2} - k_2 \frac{(\tau - \tau_0)}{2} \right\} \left| \dot{\gamma}^n \right| \tag{15}$$

One should note that the term $\left\{ \frac{\alpha \mu b}{2} k_1 - \frac{(\tau - \tau_0)}{2} k_2 \right\}$ in Equation 15 is the linear Voce hardening term (Equation 17). Having noted this, Equation 15 can also be expressed as [26]:

$$\dot{\tau} = \sum_n \left\{ \theta_0 \left(\frac{\tau_s - \tau}{\tau_s - \tau_0} \right) \right\} \left| \dot{\gamma}^n \right| \tag{16}$$

where θ_0 is the constant strain hardening rate, and τ_s represents the saturation stress in the absence of geometric effects, or the threshold stress. The hardening is defined by an extended Voce law [26], which is characterized by the evolution of the threshold stress (τ^s) with accumulated shear strain (Γ) in each grain of the form

$$\tau^s = \tau_0 + (\tau_1 + \theta_1 \Gamma) \left(1 - \exp\left(- \frac{\theta_0 \Gamma}{\tau_1} \right) \right) \tag{17}$$

where τ_0 is the reference strength, and τ_1, θ_0 and θ_1 are the parameters that define the hardening behavior [26]. The hardening law defined by Equation 17 characterizes the onset of plasticity and the saturation of threshold stress at larger strains.

The current VPSC model described by Equations 1-17 was employed to solve for the stresses corresponding to the given strains throughout the deformation. The experimentally determined initial texture of Hadfield steel (inset of Figure 2.3.2.1) was utilized as input, and the macroscopic deformation responses were predicted as presented in Figures 2.3.2.1-2.3.2.4 for all the strain rates considered in this work. The corresponding Voce hardening parameters for each strain rate are provided in Table 2.3.2.1.

Table 2.3.2.1. Voce hardening parameters utilized in the current VPSC simulations.

Strain rate (1/s)	τ_0 *[MPa]*	τ_1 *[MPa]*	θ_0 *[MPa]*	θ_1 *[MPa]*
1×10^{-1}	132	925	53×10^4	350
1×10^{-2}	132	147	43×10^3	408
1×10^{-3}	132	1580	60×10^4	390
1×10^{-4}	132	918	55×10^4	398

In order to define a proper hardening rule for the FE simulations of the impact deformation, the current VPSC model was employed to predict the equivalent stress-strain response of Hadfield steel based on the uniaxial deformation responses at all four strain rates considered herein (Figures 2.3.2.1-2.3.2.4). Specifically, the successful prediction of the experimental data (Figures 2.3.2.1-2.3.2.4) is a strong indication that the materials' deformation was successfully modeled at the micro-deformation level, and therefore, the same VPSC model was utilized to predict the equivalent stress-strain response for each strain rate utilizing the same hardening parameters for each strain rate. Since the material-independent consideration of the stress-strain distribution under impact loading (Figure 2.3.1.3) had also demonstrated that the distribution of stresses and strains throughout the sample is heterogeneous, the FE mesh for each sample was divided into three different zones with three different flow rules (Figure 2.3.1.3), such that a more homogeneous stress-strain distribution can be obtained within each zone upon impact loading. Therefore, the VPSC model was utilized to predict the corresponding equivalent stress-strain state response for each zone at all four strain rates (Figures 2.3.2.1-2.3.2.4). Specifically, the same hardening parameters as in the VPSC model predicting the experimental uniaxial deformation response were employed in all three simulations for each strain rate. The corresponding deformation of the polycrystalline aggregate within each zone was defined to the VPSC algorithm through velocity gradient

tensors, which were determined based on the material-independent strain distributions under impact loading (Figure 2.3.1.3). The corresponding velocity gradient tensors for each zone were computed as:

$$\dot{U}_1 = \begin{bmatrix} 4.2 & 1.0 & 0 \\ 1.0 & -2.1 & 0 \\ 0 & 0 & -2.1 \end{bmatrix},$$

$$\dot{U}_2 = \begin{bmatrix} 3.0 & 1.0 & 0 \\ 1.0 & -1.5 & 0 \\ 0 & 0 & -1.5 \end{bmatrix} \text{ and}$$

$$\dot{U}_3 = \begin{bmatrix} 0.3 & 1 & 0 \\ 1 & -0.15 & 0 \\ 0 & 0 & -0.15 \end{bmatrix}$$

for zones 1, 2 and 3, respectively [17].

The corresponding VPSC simulation results demonstrating the equivalent for each zone are presented in Figures 2.3.2.1, 2.3.2.2, 2.3.2.3 and 2.3.2.4 for the strain rates of 1×10^{-1} 1/s, 1×10^{-2} 1/s, , 1×10^{-3} 1/s and 1×10^{-4} 1/s, respectively. It should be noted that the strength levels attained by the equivalent deformation curves for each strain rate follows the same trend as that of the experimental uniaxial curves. This is not surprising since both the plastic deformation and the hindering of dislocations by diffusing C atoms are considered at the slip system level, where the latter leads to NSRS in Hadfield steel. Moreover, for each strain rate, higher stresses were obtained for zone 1 as compared to zones 2 and 3, and zone 3 exhibited the lowest stress levels (Figures 2.3.2.1-2.3.2.4), which stands in good agreement with the stress intensities demonstrated in Figure 2.3.1.3, where the stresses decrease as one moves from zone 1 that contains the notch towards zone 3 with the least stress concentration factors.

The results of the FE simulations incorporating the roles of microstructure and NSRS texture through crystal plasticity are presented in Figure 2.3.2.5. Even though the predictions are much better for all strain rates as compared to those of the initial FE simulations that defined hardening based on the experimental uniaxial deformation response only (Figures

2.3.1.1 and 2.3.1.2), there is an important difference between the two cases in terms of strain rate dependence. Specifically, the results of the initial simulations revealed that the best predictions were obtained by defining the flow rule for Hadfield steel based on the uniaxial deformation response recorded at the highest strain rate (1×10^{-1} 1/s in the current work), in addition to the fact that the worst predictions were based on the flow rules defined within the NSRS range. Upon incorporation of microstructure into the FE model through crystal plasticity, however; it was evident that the best prediction was obtained by defining the flow rule based on the VPSC predictions of the equivalent stress-strain response at 1×10^{-2} 1/s (Figure 2.3.2.5), which is the second highest strain rate and within the NSRS range (Figure 2.2.1). This contradictory result clearly demonstrates that reliable predictions can be obtained by proper coupling of crystal plasticity and FE analysis even if the experimental flow rule of the material is acquired under uniaxial loading and at strain rates that fall within the NSRS range. This is especially important in terms of utilizing standard laboratory experiments to characterize a material's fundamental properties, which are simple and may be restricted to strain rates within the NSRS owing to practical limitations, while predicting its deformation response under complicated loading scenarios, such as impact loading.

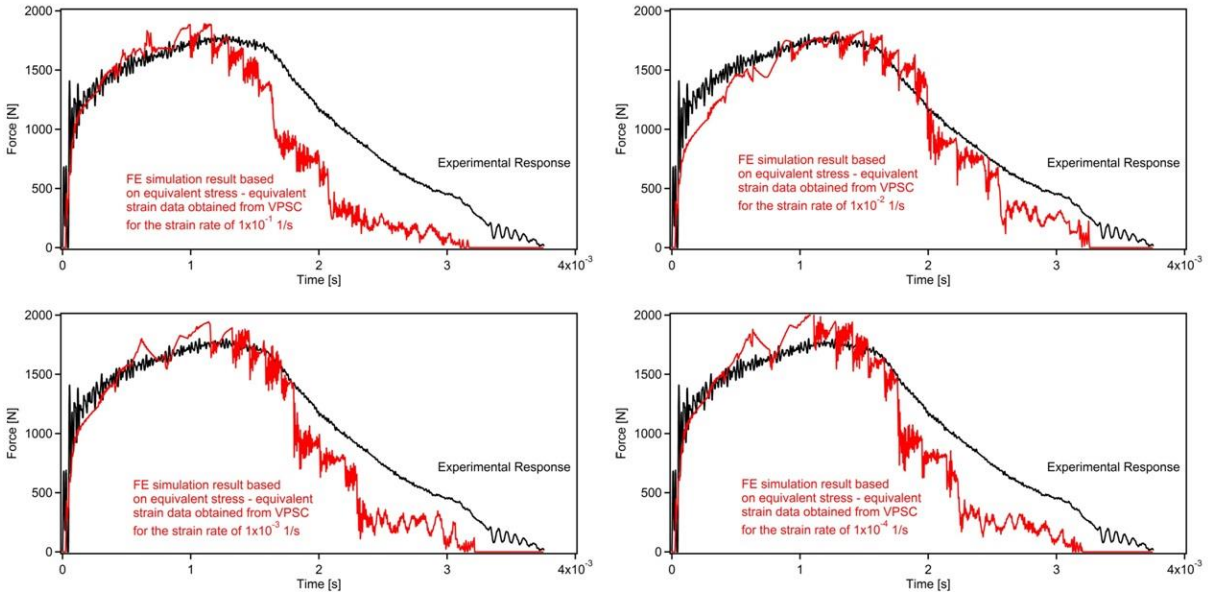

Figure 2.3.2.5. Comparison of the experimental impact response and results of the FE simulations incorporating equivalent stress-strain responses predicted by crystal plasticity for all strain rates considered.

2.4 Conclusions

The room temperature impact response Hadfield steel was studied with the aid of a multi-scale modeling approach coupling crystal plasticity and finite element (FE) analysis. The roles of texture, geometry and strain rate sensitivity were successfully taken into account all at once, where crystal plasticity was utilized to obtain the multi-axial flow rule at different strain rates based on the experimental deformation response under uniaxial tensile loading. The FE simulation results demonstrated that the utility of equivalent stress – equivalent strain response for defining the hardening rule under impact loading resulted in improved predictions. Interestingly, the simulation results indicated that a multiaxial definition of the material flow rule is the major parameter dictating the success of the predictions of impact loading deformation even in the presence of negative strain rate sensitivity, as in the case of Hadfield steel. Finally, the current set of results also demonstrated that reliable predictions can be obtained by proper coupling of crystal plasticity and FE analysis even if the

experimental flow rule of the material is acquired under uniaxial loading and at moderate strain rates that are significantly slower than those attained during impact loading. This observation opens the venue for utilizing more practical and simpler laboratory experiments to characterize a material's fundamental properties while predicting its deformation response under complicated loading scenarios, such as impact loading.

2.5 References

[1] W.S. Owen, M. Grujicic, Strain aging of austenitic Hadfield manganese steel, Acta Mater. 47 (1998) 111–126. doi:10.1016/S1359-6454(98)00347-4.

[2] O. Bouaziz, S. Allain, C.P. Scott, P. Cugy, D. Barbier, High manganese austenitic twinning induced plasticity steels: A review of the microstructure properties relationships, Curr. Opin. Solid State Mater. Sci. 15 (2011) 141–168. doi:10.1016/j.cossms.2011.04.002.

[3] E. Bayraktar, F. a. Khalid, C. Levaillant, Deformation and fracture behaviour of high manganese austenitic steel, J. Mater. Process. Technol. 147 (2004) 145–154. doi:10.1016/j.jmatprotec.2003.10.007.

[4] T. Niendorf, F. Rubitschek, H.J. Maier, J. Niendorf, H. a. Richard, a. Frehn, Fatigue crack growth-Microstructure relationships in a high-manganese austenitic TWIP steel, Mater. Sci. Eng. A. 527 (2010) 2412–2417. doi:10.1016/j.msea.2009.12.012.

[5] T. Niendorf, C. Lotze, D. Canadinc, a. Frehn, H.J. Maier, The role of monotonic pre-deformation on the fatigue performance of a high-manganese austenitic TWIP steel, Mater. Sci. Eng. A. 499 (2009) 518–524. doi:10.1016/j.msea.2008.09.033.

[6] I. Karaman, H. Sehitoglu, K. Gall, Y.I. Chumlyakov, H.J. Maier, Deformation of single crystal hadfield steel by twinning and slip, Acta Mater. 48 (2000) 1345–1359. doi:10.1016/S1359-6454(99)00383-3.

[7] I. Karaman, H. Sehitoglu, Y.I. Chumlyakov, H.J. Maier, I. V. Kireeva, Extrinsic stacking faults and twinning in Hadfield manganese steel single crystals, Scr. Mater. 44 (2001) 337–343. doi:10.1016/S1359-6462(00)00600-X.

[8] R. Ueji, N. Tsuchida, D. Terada, N. Tsuji, Y. Tanaka, a. Takemura, et al., Tensile properties and twinning behavior of high manganese austenitic steel with fine-grained structure, Scr. Mater. 59 (2008) 963–966. doi:10.1016/j.scriptamat.2008.06.050.

[9] B. Hutchinson, N. Ridley, On dislocation accumulation and work hardening in Hadfield steel, Scr. Mater. 55 (2006) 299–302. doi:10.1016/j.scriptamat.2006.05.002.

[10] S.M. Toker, D. Canadinc, a. Taube, G. Gerstein, H.J. Maier, On the role of slip-twin interactions on the impact behavior of high-manganese austenitic steels, Mater. Sci. Eng. A. 593 (2014) 120–126. doi:10.1016/j.msea.2013.11.033.

[11] D. Canadinc, H. Sehitoglu, H.J. Maier, Y.I. Chumlyakov, Strain hardening behavior of aluminum alloyed Hadfield steel single crystals, Acta Mater. 53 (2005) 1831–1842. doi:10.1016/j.actamat.2004.12.033.

[12] D. Canadinc, H. Sehitoglu, H.J. Maier, The role of dense dislocation walls on the deformation response of aluminum alloyed hadfield steel polycrystals, Mater. Sci. Eng. A. 454-455 (2007) 662–666. doi:10.1016/j.msea.2006.11.122. [13] D. Canadinc, C. Efstathiou, H. Sehitoglu, Scripta Mater. 59 (2008) 1103-1106.

[14] Y.H. Wen, H.B. Peng, H.T. Si, R.L. Xiong, D. Raabe, A novel high manganese austenitic steel with higher work hardening capacity and much lower impact deformation than Hadfield manganese steel, Mater. Des. 55 (2014) 798–804. doi:10.1016/j.matdes.2013.09.057. [15] S. Xu, D. Ruan, J.H. Beynon, Y. Rong, Mater. Sci. Eng. A 573 (2013) 132-140.

[16] J.S. Jeong, W. Woo, K.H. Oh, S.K. Kwon, Y.M. Koo, In situ neutron diffraction study of the microstructure and tensile deformation behavior in Al-added high manganese austenitic steels, Acta Mater. 60 (2012) 2290–2299. doi:10.1016/j.actamat.2011.12.043.

[17] O. Onal, B. Bal, S.M. Toker, M. Mirzajanzadeh, D. Canadinc, H.J. Maier, Microstructure-based modeling of the impact response of a biomedical niobium–zirconium alloy, J. Mater. Res. 29 (2014) 1123–1134. doi:10.1557/jmr.2014.105.

[18] Jr. J. W. Morris., Stronger, Tougher Steels, Sci. 320. (2008) 1022–1023.

[19] R. Song, D. Ponge, D. Raabe, Mechanical properties of an ultrafine grained C-Mn steel processed by warm deformation and annealing, Acta Mater. 53 (2005) 4881–4892. doi:10.1016/j.actamat.2005.07.009. [20] Y. Kimura, T. Inoue, F. Yin, K. Tsuzaki, Science 320 (2008) 1057-1060.

[21] K. Kormi, D.C. Webb, W. Johnson, The application of the FEM to determine the response of a pretorsioned pipe cluster to static or dynamic axial impact loading, Comput. Struct. 62 (1997) 353–368. [22] S.L. Raykhere, P. Kumar, R.K. Singh, V. Parameswaran, Mater. Des. 31 (2010) 2102-2109.

[22] S.L. Raykhere, P. Kumar, R.K. Singh, V. Parameswaran, Dynamic shear strength of adhesive joints made of metallic and composite adherents, Mater. Des. 31 (2010) 2102–2109. doi:10.1016/j.matdes.2009.10.043.

[23] D. Canadinc, E. Biyikli, T. Niendorf, H.J. Maier, Experimental and numerical investigation of the role of grain boundary misorientation angle on the dislocation-grain boundary interactions, Adv. Eng. Mater. 13 (2011) 281–287. doi:10.1002/adem.201000229.

[24] D. Canadinc, H. Sehitoglu, H.J. Maier, P. Kurath, On the incorporation of length scales associated with pearlitic and bainitic microstructures into a visco-plastic self-consistent model, Mater. Sci. Eng. A. 485 (2008) 258–271. doi:10.1016/j.msea.2007.08.049.

[25] R. A. Lebensohn, C.N. Tomé, A self-consistent anisotropic approach for the simulation of plastic deformation and texture development of polycrystals: Application to zirconium alloys, Acta Metall. Mater. 41 (1993) 2611–2624. doi:10.1016/0956-7151(93)90130-K.

[26] U.F. Kocks, C.N. Tome, H.R. Wenk, Texture and Anisotropy, 2nd ed., Cambridge University Press, 2000.

[27] E. Biyikli, D. Canadinc, H.J. Maier, T. Niendorf, S. Top, Three-dimensional modeling of the grain boundary misorientation angle distribution based on two-dimensional experimental texture measurements, Mater. Sci. Eng. A. 527 (2010) 5604–5612. doi:10.1016/j.msea.2010.05.037.

3 CHAPTER 5 FINAL REMARKS AND FUTURE WORK

Owing to their high strain hardening capacity, high manganese austenitic steels (HMnAS) investigated in this work are mainly used in military applications, as well as ultra-light and energy efficient constructions and vehicles. These steels have attracted attention especially within the last decade for steel and automotive industries, because they form an alternative to light-weighted alloys. Despite the increasing attention and research, the reasons for high strength and ductility of these materials remained unclear.

The motivation of the study presented herein was to improve the understanding the roles of micro-deformation mechanisms on the deformation response of HMnAS single and polycrystals deformed under tensile and impact loadings. In the first chapter the individual effects of twinning mechanism and twin-slip interactions on deformation response of high manganese twinning induced plasticity (TWIP) steels were uncovered. Calculations for distinct twin fractions of different scaled twins and critical resolved shear stress of twinning are left as future work since there is no valid adequate experimental equipment to obtain reliable data for comparison. In the second part, strain rate sensitivity effect of high manganese Hadfield steel is studied utilizing a multi-scale approach combining finite element (FE) analysis and visco-plastic self-consistent (VPSC) modeling to predict the deformation response under impact loading. Utilizing the numerical approach coupling FE and VPSC for complicated loading scenarios of different materials is left as future.

Overall, the current findings on the physics of HMnAS constitute a step forward in understanding the complicated microstructure, and open a new venue for improving the manufacturing quality and performance of new generation advanced steel grades. Moreover, introduced combined experimental and numerical methodology leads to more practical and

simpler laboratory experiments to characterize a material's fundamental properties while predicting its deformation response under complicated loading scenarios.